Utilization of X-ray Computed Tomography During the Preliminary Examination of Unopened Apollo Drive Tube Samples 73001 and 73002

Scott A. Eckley[1], Ryan A. Zeigler[2], Richard A. Ketcham[3], David Edey[3], Romy D. Hanna[3], Juliane Gross[2,4,5], Evan W. O'Neal[1], Francis M. McCubbin[2], Charles K. Shearer[6], and the ANGSA Science Team[7]

[1]Amentum – JETS2, Astromaterials Research and Exploration Science Division, NASA Johnson Space Center, Houston, TX, USA.

[2]Astromaterials Acquisition and Curation Office, NASA Johnson Space Center, Houston, TX, USA.

[3]Jackson School of Geosciences, University of Texas, Austin, TX, USA.

[4]Lunar and Planetary Institute, Houston, TX, USA.

[5]American Museum of Natural History, New York City, NY, USA.

[6]Institute of Meteoritics, University of New Mexico, Albuquerque, NM, USA.

[7]ANGSA Science Team List at https://www.lpi.usra.edu/ANGSA/teams/.

Corresponding author: Scott Eckley (scott.a.eckley@nasa.gov)

Key Points:

- X-ray computed tomography played a crucial role in the characterization of newly opened Apollo drive tubes 73001 and 73002.
- Drive tubes 73001 and 73002 sampled a large number and variety of clasts.
- Analysis of ilmenite crystals in high-Ti basalts indicates that several flows with different physicochemical conditions were sampled.

Abstract

Double drive tube 73001/2 was collected on the Light Mantle Deposit in the Taurus-Littrow Valley by Apollo 17 astronauts. It is a 4-cm diameter core that sampled up to 70 cm deep in a lunar landslide at the base of the North Massif. NASA kept these samples pristine and untouched in anticipation of advanced future analytical techniques, such as high-resolution X-ray computed tomography (XCT). Double drive tube 73001/2 was selected to be studied as part of the Apollo Next Generation Sample Analysis (ANGSA) program and was opened in November 2019 (73002) and February 2022 (73001). We discuss how XCT was utilized during the preliminary examination of these samples. This technique, which was unavailable the last time an Apollo drive tube was opened (1993), provides a three-dimensional (3-D) image of the interior of opaque objects. Prior to opening, high-resolution scans were collected of the full length of both cores, providing a novel 3-D archive of the intact lunar regolith. After opening, 352 >4 mm particles were individually bagged and scanned, allowing for their lithological classification. We provide an example of the robustness of the individual particle data by analyzing ilmenite crystals (n = 350) in fourteen high-Ti basalt particles. Our results show that ilmenite generally have highly anisotropic shapes and can take on various external morphologies, indicating that 73001/2 likely sampled several lunar basalt flows. This paper is meant to illustrate the utility of XCT for curatorial and scientific purposes during ANGSA and demonstrate its value for future sample return missions.

Plain Language Summary

Apollo 17 astronauts collected a 70-cm long and 4-cm diameter core sample of lunar regolith from the Light Mantle landslide deposit in the Taurus-Littrow Valley. NASA kept the top (73002) and bottom (73001) halves pristine so that future generations of scientists could study them with more advanced analytical techniques. As part of NASA's Apollo Next Generation Sample Analysis (ANGSA) program, 73002 and 73001 were opened in 2019 and 2022, respectively. Before opening, both cores were imaged with X-ray computed tomography (CT), a relatively new analytical technique that provides 3-D images of the interior of objects, providing the first ever 3-D image of intact lunar regolith. After opening, 352 >4 mm rock particles within the regolith were individually X-ray CT scanned, producing a catalog of high-resolution 3-D images of new lunar rock particles. We show how these data can be used to understand lunar processes, by measuring the shape and size of crystals in 3-D within some of the volcanic rock particles which reflects the physical and chemical properties of the lava. This study demonstrates how useful X-ray CT is for the characterization and analysis of sample return missions.

1 Introduction

The Apollo missions collected 382 kg of material from six different landing sites on the Moon. Since their return to Earth nearly 55 years ago, the Apollo sample suite has been extensively studied, and nearly all of the ~2200 individual samples collected have been examined as part of these studies, but a few samples (six as of 2019) were not opened or studied. These samples were saved for a future time when instrumentation and/or scientific understanding of the Moon had improved enough that the scientific return on those samples would be maximized.

With the impending return to the Moon through the Artemis program and the ~50 years of technological developments that had occurred since the Apollo samples were returned, NASA

decided it was time to open some of the previously unopened Apollo samples as part of the Apollo Next Generation Sample Analysis (ANGSA) Program. ANGSA was conceived and managed as a low-cost lunar sample return mission to prepare for Artemis. Nine NASA-selected teams, along with members from the Astromaterials Acquisition and Curation Office at NASA Johnson Space Center, were merged to form a single ANGSA Science Team that was to function as the initial sample analysis phase of a sample return mission. For a detailed description of ANGSA's objectives, team members and structure, history, and "rules of the road" see Shearer et al. (2024).

One of the unopened samples chosen for ANGSA was double drive tube 73001/2 collected by Apollo 17 astronauts. It consists of two 35-cm long by 4-cm wide aluminum tubes screwed together (73001 = lower; 73002 = upper) that sampled up to 70 cm deep into the Light Mantle landslide deposit at the base of the South Massif in the Taurus-Littrow Valley. The 73001 portion of the Al double drive tube was sealed under vacuum on the lunar surface in a stainless steel Core Sample Vacuum Container (CSVC), whereas the 73002 portion of the Al double drive tube was unsealed. Both were returned to Earth in an Apollo Lunar Sample Return Container (ALRSC) and promptly examined in a N_2 purged glove box at the Johnson Space Center (JSC). 73001 was sealed into a larger vacuum container almost immediately after the initial examination, whereas 73002 was triply sealed in Teflon bagging and imaged by a medical X-ray scanner at JSC (Fig. 1), which revealed clasts of different sizes, void spaces, and that the Al tube was not filled. Both samples were stored in the lunar sample vaults untouched under N_2 purge conditions by NASA until they were opened (73002 = 2019; 73001 = 2022). Further details about the storage of 73001 and 73002 and the preparation underwent by curation to prepare for dissection of the core samples are provided in Gross et al., (this issue).

A primary objective of the ANGSA Science Team was to conduct a preliminary examination (PE) of double drive tube 73001/2 and, in parallel, to conduct objective-driven scientific investigations of the samples. The main task during the PE phase was to dissect the cores and produce a sample catalog with sufficient detail that members of the scientific community can make informed requests about the samples they will need to execute scientific investigations. Aside from the X-ray image taken of 73002 in 1973, these samples were unstudied, but expected to have a mixture of lunar lithologies since it was taken from a landslide deposit at the base of the 2300-m tall South Massif. Therefore, to maximize the information gained from these samples during PE and produce a high-fidelity sample catalog, X-ray computed tomography (XCT), a relatively new analytical technique for geological samples that was not available for previous double drive tubes, was added to the PE procedure. Whole-core XCT scans taken prior to extrusion and dissection would produce a high-resolution three-dimensional (3-D) archive of the 73001/2 stratigraphy, as well as provide a 'roadmap' during the dissection process. Individual scans of clasts removed during dissection could enable lithological classification and provide even higher resolution images for follow-up scientific analyses.

X-ray computed tomography is a nominally non-destructive technique to image the interior of opaque objects in three dimensions. In lab-based XCT systems, X-rays emanate from a source and pass through the object being scanned, and are attenuated to different degrees. The intensity of the partially-attenuated beam is detected and recorded as a single two-dimensional (2-D) X-ray projection image (i.e., radiograph). This process is repeated thousands of times as the sample incrementally rotates 360°. The projection images are mathematically reconstructed into a 3-D grid of voxels (i.e., a pixel with a 3rd dimension; often cubic) mapping differences in

the effective linear X-ray attenuation coefficient. Each voxel is assigned a CT number (CT #) that reflects the effective X-ray attenuation coefficient of the material comprising that volume. The X-ray attenuation coefficient varies as a function of average atomic number, density, and X-ray energy. Voxels that are assigned higher CT #'s (i.e., more X-ray attenuating) are generally visualized with brighter grayscale values. For reviews about CT data acquisition and processing, see (Cnudde & Boone, 2013; Ketcham & Carlson, 2001; Withers et al., 2021).

X-ray CT scanning is uniquely suited for the analysis of priceless and irreplaceable samples such as astromaterials due to its nominally non-destructive nature and the ability to image through sample containers (e.g., bags and tubes) that maintain their pristineness. However, there are some potentially negative side effects. The natural radiation record is eradicated, preventing thermoluminescence measurements (Sears et al., 2016; Sears et al., 2018). Investigations are ongoing to assess the effects of XCT on organic compounds in samples, but preliminary results are promising (Friedrich et al., 2019; Glavin et al., 2024; Hanna & Ketcham, 2017). Despite these potential effects, the role of XCT to better understand the origin and evolution of astromaterials has expanded significantly in recent years. See Hanna and Ketcham (2017) for a review of the application of XCT to planetary materials.

Studies of lunar samples using XCT have provided new perspectives and insights into geological processes on the Moon. The petrogenesis, volatile history, and relative locations within host lava flows have been explored in several Apollo high-titanium (Gawronska et al., 2022; Wilbur et al., 2023) and low-titanium (Wilbur et al., 2025) basalts by investigating 3-D crystal and vesicle abundances, sizes, shapes, and orientations. Measurements of lunar regolith particle composition, shape, size, and porosity by XCT have improved upon those made in two-dimensions (2-D) and show that continued impact fragmentation events tend to produce more equant particles, and that there is a correlation between particle shape and lithology (Katagiri et al., 2015; Tsuchiyama et al., 2022). Agglutinate particles are generally the most irregularly shaped (Katagiri et al., 2015) and can preserve textural and compositional evidence for a single impact event (Huang et al., 2024). Similar studies have focused on enhanced 3-D characterization of lunar regolith and simulants to better understand and recreate, respectively, their physical properties for future lunar exploration (Goguen et al., 2024; Wilkerson et al., 2024).

ANGSA is NASA's first "sample-return mission" to systematically use XCT during its preliminary examination phase. In this paper, we: (1) document how XCT data of Apollo drive tubes 73001 and 73002, and particles subsequently extracted from them, were acquired and processed; (2) demonstrate the value of these datasets during preliminary examination; and (3) showcase an example of the utility of these data for scientific purposes. This paper is not intended to be a complete scientific investigation of these datasets, as this is outside the role of ANGSA's preliminary examination phase. We expect this endeavor to continue for years into the future and to be shared by the lunar science community as more questions about these samples arise. Instead, this paper is an outline of the benefits and challenges of incorporating XCT into preliminary examination, a case study of how these 3-D datasets can provide valuable insights into questions that have typically been addressed with 2-D datasets, and a roadmap for future sample return missions.

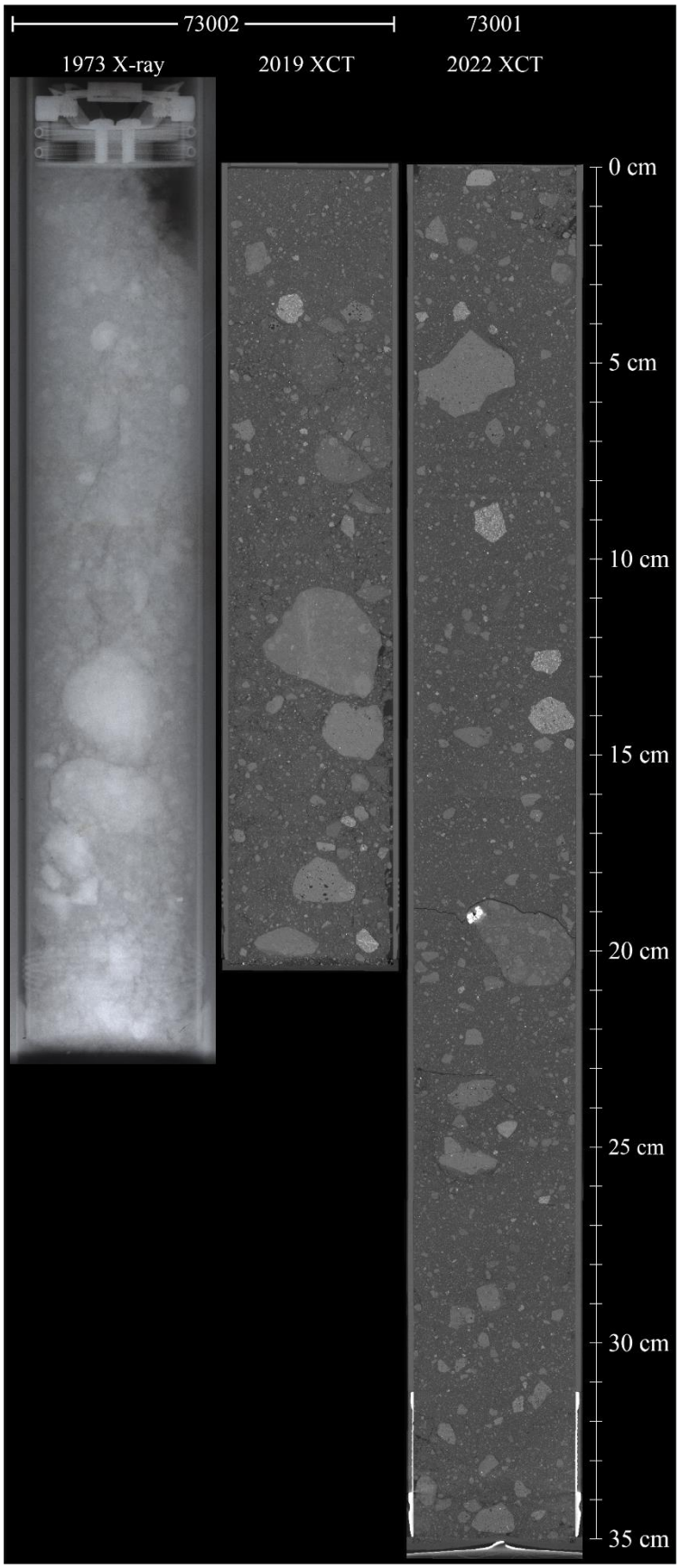
73002
73001
1973 X-ray
2019 XCT
2022 XCT
0 cm
5 cm
10 cm
15 cm
20 cm
25 cm
30 cm
35 cm

Figure 1. Whole-core X-ray images of 73001 and 73002. (Left) X-ray radiograph taken of 73002 in 1973. (Middle and Right) Grayscale XCT slices through central sections of 73002 and 73001 using the 2x down-sampled datasets (voxel size = 25.8 µm). The difference in 73002 core length between the 1973 radiograph and 2019 XCT scan was due to intentional manual compaction (see Gross et al., this issue).

2 Methods

2.1 Whole-core scanning

Both cores were taken to the University of Texas High-Resolution X-ray Computed Tomography (UTCT) Facility for high-resolution, whole-core scanning. Core 73002 was scanned in October 2019, and 73001 in March 2022. Both cores were scanned using an instrument custom-designed by North Star Imaging (NSI), using a Feinfocus FXE 225.48 microfocal X-ray source and a 2048 x 2048 pixel Perkin Elmer flat panel detector. To achieve maximum spatial resolution, the NSI Subpix™ capability was used, in which four overlapping datasets are gathered with half-pixel vertical and horizontal offsets of the detector, effectively doubling the detector size to 4096 x 4096 pixels, resulting in a voxel edge length of 12.9 µm for both scans. Data were acquired as a series of individual cone-beam volume scans, with overlap to aid in stitching them together to create a continuous dataset for each core.

2.1.1 73002

Core 73002 was triple-bagged in Teflon in the lunar curation gloveboxes at NASA JSC in preparation for scanning at UTCT. It was mounted vertically in a plexiglass tube fixed to the scanner's rotation stage (Fig. S1). The X-rays were set at 180 kV and 0.18 mA and pre-filtered with 0.72 mm of aluminum. To complete scanning within time limits, each Subpix™ sub-volume acquisition was done with continuous rotation. Preliminary X-ray radiographs revealed that regolith filled approximately 20 cm of the tube, which would require scanning in six sub-volumes, with ~500 slices of overlap between adjacent volumes to avoid cone-beam artifacts. Each sub-volume acquisition took approximately 2.3 hours to collect.

The continuous-rotation acquisition was slightly incompatible with the state of the Subpix™ software at that time, and the four data sets for each volume were rotationally mis-aligned from each other by up to 0.35°, resulting in a blurred reconstruction. Sharpness was recovered by manually re-aligning the raw projection images using bash scripts. A software beam-hardening correction was applied during reconstruction.

2.1.2 73001

Core 73001 was vacuum-sealed in a stainless-steel outer sleeve (CSVC) by astronauts on the Moon and kept sealed until February 2022, where the bottom was pierced and gases extracted (Gross et al., this issue). The top and bottom of the CSVC were X-ray CT scanned at NASA JSC to determine the size and location of the pierced hole, as well as to collect images of unopened CSVC In-Ag metal knife edge seals for engineering purposes. These scans revealed that the core was over-filled on the Moon, resulting in poor seating of the "keeper" inside the inner aluminum tube (see Gross et al., this issue for a description of the 73001 CSVC). It was thus decided to leave the core in its stainless-steel outer sleeve surrounded by triple-bagged Teflon for scanning

at UTCT.

This unexpected setup necessitated a number of changes to the scanning conditions compared to 73002. The core was positioned for scanning in a custom PVC tube mount (Fig. S1). X-ray energy was increased to 190 kV and current held at 0.18 mA, and no beam filter was used, in an attempt to compensate for the steel sleeve effectively serving as a more severe filter than the 0.72 mm aluminum filter used for 73002. Gantry positions were adapted to allow the steel outer sleeve to be mostly excluded from the scan field of view and achieve the same voxel size as 73002. For this scan, non-continuous rotation was used, avoiding the rotational mismatch issues from 73002. Preliminary X-ray radiographs revealed that regolith filled the entire 35 cm tube. The core was scanned in nine sub-volumes, unfortunately with a lesser degree of overlap (~180 slices) than was used for 73002, as the configuration changes led to miscalculation of the offset necessary for avoiding cone-beam artifacts at the top and bottom of each scan volume. Additionally, due to core tilt the steel outer sleeve was sometimes within the scan field of view and sometimes out of it, resulting in a variable artifact around the core margin. Similarly, a steel wire attached to the steel tube, twisting around the length of the core, cast a secondary beam hardening and scattering artifact that resulted in uneven brightness in the reconstructed data. Finally, the steel cap caused additional beam hardening and scattering artifacts. These cumulative effects, shown on the left side of Figure 2, significantly affected CT numbers, and complicated estimating an optimal beam-hardening correction factor, so the value for the 73002 scan was re-used. Each sub-volume took approximately 4.6 hours to collect.

2.2 Whole-core scanning corrections

The sub-volume scans for each core were reconstructed individually, and then stitched together to create a single cohesive dataset for the entire length. Reconstruction parameters were selected so that no lithologic components were at the limiting values of the unsigned 16-bit output scale (0, 65535). Both scans were corrected for ring artifacts before further processing using methods created at UTCT (Ketcham, 2006).

2.2.1 Stitching-related corrections

During stitching of cone-beam image volumes for core 73002, a dimensional inaccuracy in the scan plane of 5-7 pixels (64-90 µm) was noted between the top of one scan and the overlapping bottom of the next, probably owing to a slight miscalibration of the gantry and source-detector configuration. To address this, slice images in each volume were progressively isometrically rescaled so all matched the mid-volume slice, using scripts in the IDL programming language. Each volume was also translated and rotated to match the prior one, utilizing the SIFT algorithm (Lowe, 2004) in ImageJ (Schneider et al., 2012) to find the transformation matrix. Finally, there was also a continuous change in CT numbers (image gray levels) from the top to the bottom of each cone-beam acquisition. In the version of the 73002 data initially released in 2020, this was corrected by rescaling so that overlapping slices matched using a second-degree polynomial to characterize the CT number progression from the top to the bottom of each stack. Core 73001 required the same geometric correction as 73002, but CT numbers were not adjusted at this stage owing to complications stemming from other artifacts.

To improve data continuity between individual sub-volume scans, a series of slices in the overlap regions were linearly averaged. Nine overlapping slices were used for 73002, and 80 for 73001 as a part of addressing the insufficient-cone-beam-overlap issue.

2.2.2 CT number corrections

2.2.2.1 Core 73001

The severe artifacts for 73001 required extensive corrections to maximize the fidelity of the CT numbers. All corrections were written as IDL functions, and were designed to identify and eliminate artifacts using continuous functions that varied systematically along the core length. Due to the size of the data (711 GB), corrections were first designed and calibrated using down-sampled versions of the data set, and then applied to the full-resolution data.

The corrections took advantage of the aluminum tube wall as a consistent feature that should have the same attenuation everywhere. As an initial step, to address the tilt of the core tube, the core center was located across all slices by fitting a circle to the inner diameter of the aluminum sleeve. The progression in center position for 73001 was roughly linear, with horizontal and vertical displacements of ~3.3 and ~1.6 mm, respectively (Fig. S2). The subsequent sequence of corrections is summarized in Figure 3.

To quantify the CT number errors, averages were calculated radially along the tube inner diameter, along an outer annulus of the outer 15% of the core radius, and around a circle encompassing the inner 50% of the core radius (Fig. 3B). The variation in tube wall values was due to a number of artifacts at scan stitching areas due to cone-beam artifacts and primarily from the steel outer tube and wire being variably in and out of the scan field, but other contributing factors likely included scattering inside the X-ray cabinet and source variation. The offset between the outer and inner parts of the core material reflects scattering and beam hardening artifacts, though local variations are caused by large clasts with higher density and variable lithology, particularly in the central region.

The artifact from insufficient cone-beam overlap consists of progressive radial darkening, with some blurring, growing from the image edges toward the center as the bottom or top of a cone beam acquisition is approached (Figs. 3A, S2). The artifact is centered in the scan field of view, but off-center with respect to the core material, due to the tilt of the inner sleeve. The radial progression and magnitude of the darkening was measured at each interface between cone-beam volumes, by comparing the average grayscale in this region to those on slices just beyond the stitched region, which contained similar albeit somewhat different material due to sample heterogeneity. A functional form for the cone-beam artifact sought that would allow for straightforward interpolation from slice to slice, and was found empirically as: $f_{CB}(r)=C_0 \tanh(C_1 (r-C_2))$, where C_0 is magnitude, C_1 radially scales the tanh function, and C_2 is the artifact inner radius (Fig. S3). The artifact was modeled with the inner radius increasing linearly and magnitude decreasing linearly with vertical progression up and down from the center of overlap. Optimal values for all parameters were found by a combination of fits to the measured data and manual adjustment. This correction was applied to all stitching zones prior to further processing (Fig. 3C).

Removing grayscale variations due to beam hardening and scattering was done by utilizing the innermost annulus of the sleeve as an effective attenuation standard to normalize gray levels both radially and along the core. The asymmetric effect of the steel sleeve being incompletely in the scan field, and steel wire between sleeves, was characterized using the first three components of a Fourier expansion, $f_{ASYM}(\theta) = M_0 + M_1 \sin(\theta + A_1) + M_2 \sin(2\theta + A_2) + M_3 \sin(3\theta + A_3)$, where M and A are the magnitude and angular offset for each Fourier component (Fig. S4). Values for these seven terms were fitted for the inner sleeve annulus of each slice

image. The three Fourier components had magnitudes reaching up to ~1000, ~300, and ~150, respectively, excluding the region of the steel-covered end (Fig. 3D). These curves were used as the basis for a correction that scaled linearly from ~25% of the core radius to the outer portion of the aluminum sleeve. The sleeve could not be used for normalization at the steel-covered end, and so the Fourier magnitudes and offsets were extrapolated from the adjacent Al-enclosed section.

Removal of the asymmetric artifact revealed that the software beam-hardening correction applied during reconstruction had slightly over-corrected the data, making the core center brighter than its rim. The fall-off in CT numbers also affected the outer portion of the Al tube in a way that was consistent with the core material. To quantify this, sets of 100 slices with minimal clasts were used to calculate radial sums of CT numbers, revealing that the radial extent of the artifact was consistent but its magnitude was not along the length of the core (Fig. S5A), again due to the varying effects of the steel sleeve and wire. This effect was fitted with an empirical function of the form: $f_{BH}(r_c) = C_0(1\text{-}\exp(C_1 r_c))$, where r_c is the radial distance from the core center, C_0 scales the magnitude, and C_1 scales the radial extent. Values for C_0 were fitted manually, and a second-degree polynomial was used to characterize how it varied along the length of the core (Fig. S5B).

The stainless-steel cap caused severe beam-hardening and scattering artifacts that required another custom correction. The principal artifact was a steep rise in gray levels toward the steel rim, with an extent and severity that varied with steel thickness (Fig. S6). The artifact was characterized by fitting another beam-hardening function $f_{BHS} = C_0 \exp(C_1 r_c^{C2})$ in three locations with two different steel thicknesses. These were interpolated radially based on steel thickness, which was measured at 2° angular intervals in each slice to allow the correction to vary locally. This correction was notably incomplete, as X-ray scattering led to light and dark artifacts that propagated diagonally through the core that appear as diffuse rings (Fig. S5, right column); CT numbers in these regions should be used cautiously.

The corrections f_{ASYM} and f_{BH} or f_{BHS} were combined into a single correction map for each slice, that was then subtracted from the data. This correction made the average aluminum value 10050 down the tube, and the characteristic CT numbers of the core and rim regions of the core material had been made consistent (Fig. 2 right side; Fig. 3E,F). Finally, a circular mask was used to remove everything more than a few voxels beyond the aluminum inner sleeve.

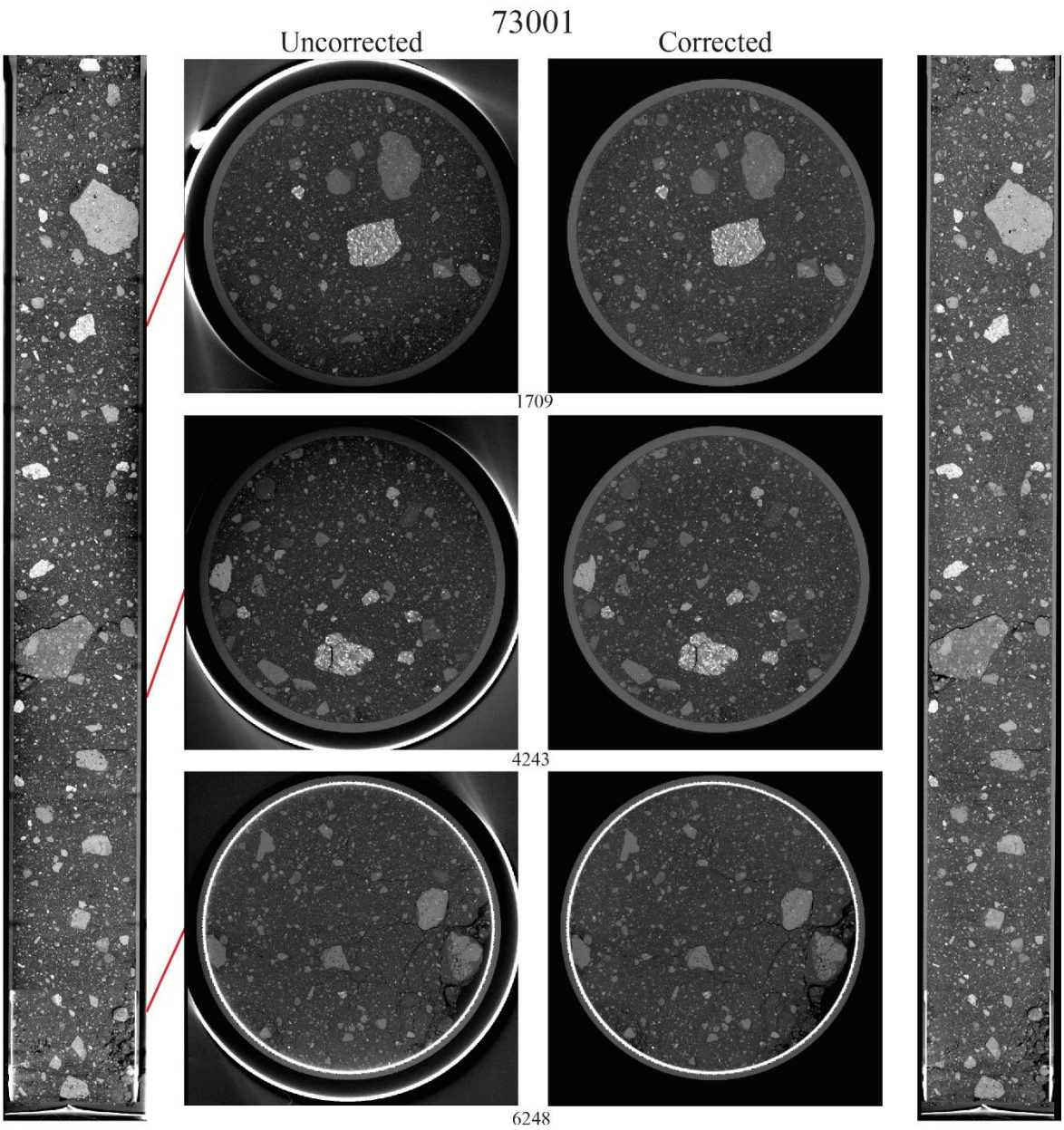

Figure 2. Example uncorrected (left side) and corrected (right side) images from core 73001. Tall images are resliced data sets along core length (35 cm). Field of view for CT images is 4.80 cm. Numbers are slice numbers in 4x-downsampled data. The bright arc along the outside of the uncorrected slices images is the steel outer sleeve, and the wire is visible in the 1709 slice image. Omitting the steel from the scan field led to an artifact of brightening on one side and darkening on the other, requiring specialized correction.

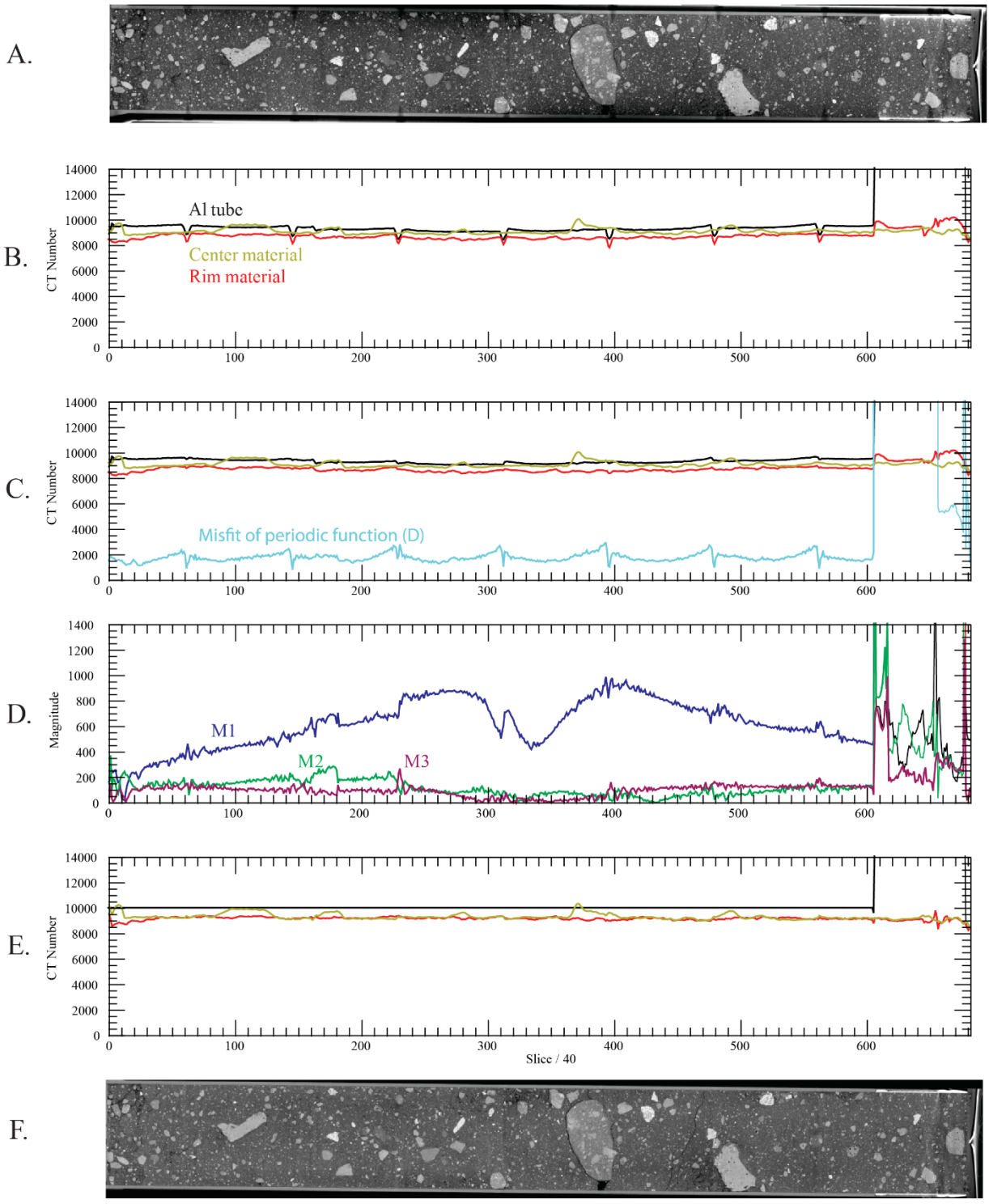

Figure 3. Correction sequence for core 73001. (A) Uncorrected cross-section image (35 cm long), showing progressive variation due to steel sleeve, as well as cone-beam artifacts where different scan volumes were stitched together. (B) Variation in annular average of CT numbers around Al tube inner rim, the outer radial 15% of the core, and the inner radial 100% of the core. Values calculated at 10-slice intervals in 4x-downsampled data. Intermittent variations are due to clasts in the regolith, particularly in the inner portion. (C) Annular averages after correction

for cone-beam artifact at stitching points. Cyan curve shows the misfit of the periodic functions used to characterize CT number variation around the Al tube inner rim; the magnitudes of the three Fourier components are shown in (D). (E, F) Annular averages and cross section image after all corrections applied.

2.2.2.2 Core 73002

Re-inspection of the CT data for core 73002 after the completion of corrections for 73001 revealed previously unrecognized shortcomings in the previously released data. The along-core consistency of grayscales from scan to scan showed some drift, possibly due to changing beam conditions and/or detector efficiency during the scans, and the beam-hardening correction showed room for further improvement. Furthermore, the different scanning conditions and corrections for each had led to the CT numbers for the two cores being inconsistent with each other, complicating study of regolith properties across them.

To begin the process, the 16-bit data were cropped from 3721 pixels on a side to 3600, omitting regions that did not include the core, reducing data size, facilitating even downsampling, and providing a straightforward indicator separating the resulting corrected data (i.e., 73002-revised) from the earlier version (73002-original). The migration of the core center due to tilt was traced, and it was found to follow a slightly curved path (Fig. S2), probably due to imperfect machining of the tube, as the inner diameter was not fully centered in the outer diameter.

Calculating annular averages for the Al tube and outer and inner core material was complicated by the condition of 73002. Due to spillage during collection (Gross et al., this issue), parts of the rim area have considerable void space (Fig. 4). Similarly, much of the regolith is disrupted, making it an irregular combination of regolith and void along the core. These effects were diminished by omitting CT numbers below 7500 (corresponding to disrupted regolith) and using the mean instead of the median for the remaining voxels in each set. This resulted in the progression shown in Figure 5B. The test for asymmetric artifacts showed that they are relatively minor, with magnitudes of all three Fourier terms of less than 100 within the core, except the bottom where a plastic cap was partially omitted from the scan field of view (Fig. 5C).

The disruption in the core also complicated isolating residual beam-hardening effects persisting after the correction applied during reconstruction. The optimal area for this was judged to be the uppermost section of the core, where the regolith material was re-consolidated when the keeper was tightened in preparation for transport and scanning at UTCT. Radial averaging in this area showed that the central region is slightly darkened compared to the rim (Fig. 5B, down-sampled slices 5-40); the apparent cross-over to the center being more attenuating at higher slice numbers can be traced to the increasing amount of disruption affecting the rim more than the center. At the same time, the outer part of the Al tube is darker than the inner, representing an inversion of the beam-hardening artifact that can often occur when using a reconstruction-based correction. A simple correction was constructed as a two-part radially symmetric function, with a linear correction from the center to the edge of the regolith, with scaling based on the tube brightness in that slice, followed by a second-degree polynomial that performed an essentially cosmetic correction on the Al tube (Fig. S7).

Finally, a rescaling was calculated to maximize the consistency of the data with 73001.

Average CT numbers were measured in vesicles and various components of Ti-basalts (ilmenite, pyroxene, and plagioclase) and undisturbed regolith to construct a linear correction. Rescaling the 73002 CT numbers using a second-degree polynomial (Fig. S8) resulted in the CT numbers for all phases agreeing across data sets to within 70, or about 0.1% of the 16-bit scale.

The asymmetric and beam-hardening corrections and rescaling were combined and applied to the 73002 data, followed by a circular mask to remove unnecessary features beyond the Al tube. The resulting down-tube averages are shown in Figure 5D, and example corrected images are shown in Figure 4 (right side) and Figure 5E. The apparently greater brightness of the center compared to the rim can be attributed to rim relatively being more disrupted; this was confirmed in a number of locations by measuring the average CT number of clasts of the same lithology at varying radial positions.

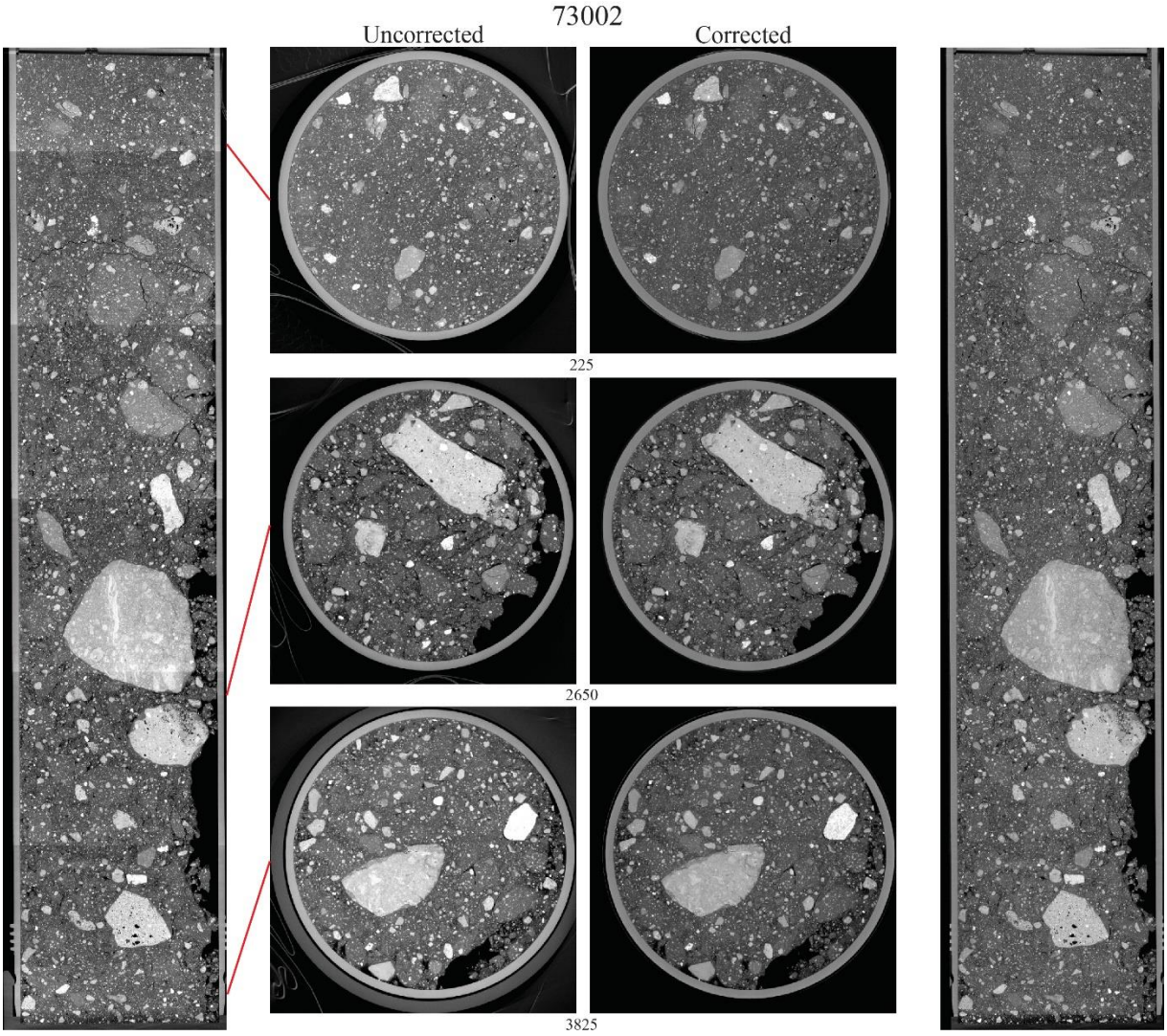

Figure 4. Example uncorrected (left side) and corrected (right side) images from core 73002. Tall images are resliced data sets along core length (20 cm). Field of view for CT images is 4.64 cm. Numbers are slice numbers in 4x-downsampled data. Uncorrected data shows CT numbers steadily increasing downward in each of the six cone-beam scans taken to span the core. Material through much of the core is disrupted doe to spillage during collection, and subsequent

movement during handling.

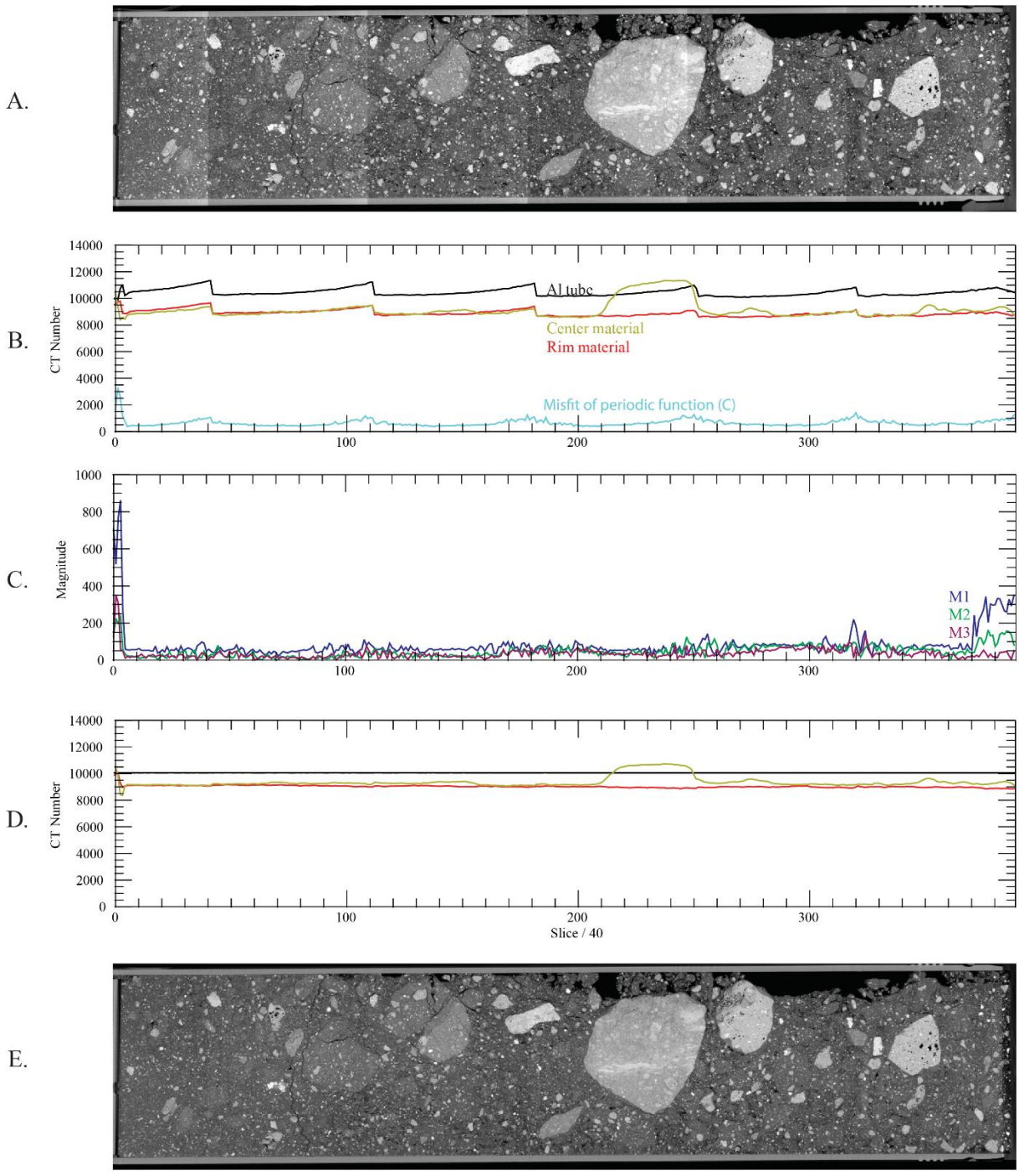

Figure 5. Correction sequence for core 73002. (A) Uncorrected cross-section image (20 cm long). (B) Variation in annular average of CT numbers around Al tube inner rim, the outer radial 15% of the core, and the inner radial 100% of the core. Values calculated at 10-slice intervals in 4x-downsampled data. Intermittent variations are due to clasts in the regolith, particularly in the inner portion. Cyan curve shows the misfit of the periodic functions used to characterize CT

number variation around the Al tube inner rim; the magnitudes of the three Fourier components are shown in (C). (D, E) Annular averages and cross section image after all corrections applied.

2.3 Individual particle scanning

After whole-core scanning, both drive tubes were opened and the soil was carefully extruded on its side into a custom holder so as to maintain as much of the original three-dimensional context as possible. The soil was then meticulously dissected and any particle >4 mm (in passes 1 and 2 and >10 mm in pass 3) was named, weighed, imaged, and individually bagged with three layers of Teflon, all within a N_2-purged glovebox. For a detailed description of the extrusion and dissection processes, see Gross et al., (this issue). Each individually bagged >4 mm particle was removed from the cabinet and XCT scanned at the Astromaterials X-ray Fluorescence and Computed Tomography (X-FaCT) Laboratory at NASA JSC using a Nikon XTH 320 large cabinet scanner equipped with a 180 kV nano-focus transmission tungsten target source and a 2000 x 2000 pixel Perkin Elmer CCD flat-panel detector. The bagging was twisted around each particle and pushed into and suspended within cylinders of different sizes made of low-X-ray-attenuating materials (i.e., plastic or carbon fiber) for scanning. Great care was taken to avoid popping any of the triplicate bagging. This mounting method was generally successful except for the occasional sample movement during scanning caused by rebound from the relatively stiff Teflon bagging.

Scanning conditions were optimized for each sample, but X-ray tube settings varied from 90 kV to 155 kV and 2.0 W to 5.0 W. All scans rotated 360° with 1891 to 3141 projections per rotation and 1 s to 2 s exposure per projection. Scans took approximately 1 to 2 hours. Voxel sizes varied from 2.81 to 22.58 µm/voxel edge. Projection images were reconstructed into a three-dimensional volume using Nikon's CTPro3D (v. 5.4) proprietary software where mathematical corrections were implemented to reduce beam hardening artifacts. The reconstructed datasets were exported as a contiguous series of 16-bit grayscale TIFF images which, when stacked together, comprise a 3-D volume. The name, mass, classification, relevant scanning information, and a video of the CT TIFF stack can be found for every sample in Appendices 5 and 6 of the ANGSA Sample Catalog (https://curator.jsc.nasa.gov/lunar/angsa_catalog.cfm).

2.4 3-D analysis of ilmenite in high-Ti basalt particles

As a demonstration of the unique textural analysis possibilities enabled by XCT data, we conduct a novel 3-D analysis of lunar ilmenite crystals. Ilmenite is a ubiquitous phase within high-Ti basalts and is easily distinguished from other phases. However, there are thousands of ilmenite crystals in each particle and almost all of them are three-dimensionally connected. Ideally, we would measure them all, but manually inspecting, delineating, and separating every crystal-crystal contact in 3-D for each crystal is not feasible, and no automatic method to do this for such an intergrown and complex system is currently available. Instead, we take on a more realistic approach by measuring the 3-D crystal habit axial lengths of a representative population (n = 25) of ilmenite in fourteen (10 from 73001; 4 from 73002) high-Ti basalt particles showing a variety of textures.

Ilmenite crystal habit axial lengths were manually analyzed following the procedure from (Eckley et al., 2024a). The XCT data were visualized and measured using Dragonfly™ software (Comet Technologies), which allows the analyst to navigate the dataset in three views using

cross-hairs that can be dynamically repositioned and reoriented so that the entire sample can be viewed and sliced along any angle at every location. First, a random ilmenite crystal was selected and the cross-hairs iteratively repositioned and reoriented until a central slice along its longest axis was exposed. The next view was oriented at an angle orthogonal to the longest one to show a central slice along the shortest axis. The final view was oriented orthogonally to the first two to expose a central slice along the intermediate axis. The long, intermediate, and short axis crystal habit lengths were measured using the 'ruler' tool. Once measured, we randomly reoriented the dataset using the 'cine' tool, another random crystal was picked, and the process repeated 25 times.

We assessed the uncertainty of our method with six replicate analyses of a single very elongated, very platy, and equant crystal in three different samples (73001,181B, 73002,1017B, and 73002,80A, respectively). The relative uncertainties (1 relative standard deviation) of the long, intermediate, and short axis replicate measurements are: very elongated (1.1%, 10.2%, and 23.4%, respectively); very platy (1.5%, 2.8%, and 11.1%, respectively); and equant (2.4%, 4.0%, and 8.2%, respectively). The average uncertainty for all replicate analyses is 0.015 mm (1rsd = 7.2%), which corresponds to ~4 voxel lengths (the average voxel length for the measured samples is 0.00399 mm). Additional potential sources of uncertainty come from natural variation of the crystals. Some very elongated crystals are doubly terminated so we measured the longest termination, and some very platy crystals have small outgrowths on their edges, which were not included in the measurements. Most crystals are touching at least one other crystal and many are highly aggregated, so grain boundaries needed to be delineated by the analyst. This is done by viewing the crystal at different locations and along several orientations and using petrographic features within a crystal, such as internally uniform fracture patterns and compositional zoning. In the rare case where crystal boundaries could not be defined, that crystal was ignored. Only fully enclosed crystals (i.e., not truncated by the sample boundary) were measured.

3 Results

3.1 73001 and 73002 whole-core datasets

Whole-core XCT scans revealed that regolith filled 34.9 cm of 73001 and 20.1 cm of 73002 (Fig. 1). Because of their lengths and the high spatial resolution (12.9 µm/voxel edge) of the XCT scans, the final reconstructed datasets for 73001 and 73002-revised include 27,600 slices (711 GB) and 15,800 slices (381 GB), respectively, oriented orthogonally to the core length. Each slice for 73001 is 3721 x 3721 pixels, which 73002-revised was cropped to 3600 x 3600 pixel without losing information. The combined length of 73001 and 73002-revised is made of 43,400 slices and 1,092 GB of data. Due to the bulkiness of these datasets, smaller versions were also produced by down-sampling the full-resolution dataset by 2x and 4x along the X, Y, and Z orientations (Table 1). The 2x and 4x datasets are suitable for most purposes, but the full-resolution (referred to as 1x) dataset is ideal for visualizing fine-grained features, such as igneous textures within a high-Ti basalt clast shown in Figure 6. However, most desktop computers cannot open the entire length of the 1x datasets due to hardware limitations, so viewing focused sub-volumes is advised.

Sample	Dataset	Voxel size (µm)	Data Volume (GB)	Slice dimensions (XY)	No. of slices (Z)

73001	1x	12.9	711	3721 x 3721	27,600
	2x	25.8	89	1861 x 1861	13,800
	4x	51.6	11	931 x 931	6,900
73002 - Original	1x	12.9	408	3721 x 3721	15,820
	2x	25.8	48	1776 x 1772	8,252
	4x	51.6	6	888 x 886	4,126
73002 - Revised	1x	12.9	381	3600 x 3600	15,800
	2x	25.8	48	1800 x 1800	7,900
	4x	51.6	6	900 x 900	3,950

Table 1. Voxel size, data volume, slice dimensions, and number of slices for whole core XCT datasets for 73001, 73002-original, and 73002-revised. 1x = full-resolution dataset. 2x = down-sampled by two in X, Y, and Z. 4x = down-sampled by four in X, Y, and Z.

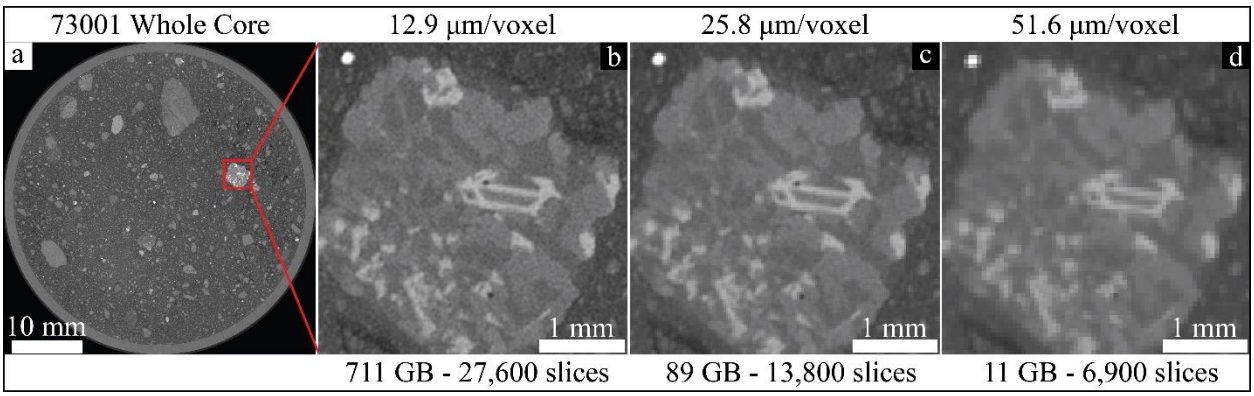

Figure 6. Comparison of 1x, 2x, and 4x whole-core XCT datasets. A single grayscale CT slice of 73001 (a) and grayscale CT slices (b – d) of the same basaltic clast (outlined in red box) from the different resolution datasets (b = 1x, c = 2x, d = 4x).

These datasets were invaluable during the opening, extrusion, and dissection processes. They revealed that large void spaces existed in 73002, which influenced how the sample was to be oriented during extrusion to avoid slumping of the core material (Gross et al., this issue). The sample processors were also able to cross-reference the XCT data during dissection to help predict what clasts were to be expected at specific locations. They were also able to identify and locate soil clods, which typically did not survive the dissection process. The morphology and composition of these soil clods, which may reflect processes that affect lunar regolith, are only preserved in the whole-core XCT datasets.

In addition to supplying crucial information to the sample processors during preliminary examination, these data provide a novel and permanent 3-D record of the lunar subsurface up to 70 cm deep. The core material is made of rock, mineral, and glass fragments within fine-grained

soil. There are also void spaces and fractures. See supplementary videos (S1 and S2; Eckley, 2025) to view the whole-core 2x down-sampled XCT datasets. The main types of fragments are lithic clasts, mineral and glass clasts, and soil clods, or 'peds' based on formal soil nomenclature, that exist at a wide range of sizes from up to ~33 mm in 73001 and up to ~30 mm in 73002 down to the scan resolution. Lithic, mineral, and glass clasts are generally angular and frequently rimmed with fine-grained regolith material. They occur as a variety of different lithologies and mineral phases. Peds are angular to rounded and are three-dimensionally coherent domains of soil and sub-fragments. They are distinguishable from the surrounding soil and fragments by usually having slightly higher CT numbers. The cause of the different CT numbers is not resolvable but probably reflects differences in bulk density where the soil within peds is more densely packed. We observe no apparent layering, sorting, or preferred orientation of fragments. However, a more detailed object-based analysis is required to confirm this observation. An analysis of clast size distribution in 73002 is reported by Magnarini et al., (this issue) where they found there are fewer large clasts (>1 cm) in the upper 5 to 10 cm of the 70 cm core.

3.2 Individual particle classification

There were 352 >4 mm rock fragments from 73001 (n = 220) and 73002 (n = 132) that were individually XCT scanned. The name, dissection pass and interval, mass, lithology, and a short description of each sample are found in Appendix 5 of the ANGSA Sample Catalog (https://curator.jsc.nasa.gov/lunar/angsa_catalog.cfm). Particles were classified and described by the lunar sample curator (R. Zeigler) and deputy lunar sample curator at the time (J. Gross) using the XCT data and their years of lunar sample knowledge. The XCT data show relative differences in X-ray attenuation. Generally, objects with brighter grayscale values (i.e., more X-ray attenuating) are denser. The samples were classified into one of nine major lithologic categories – agglutinate, anorthosite, high-Ti basalt, low-Ti basalt, granulite, impact melt, impact melt breccia, regolith breccia, and soil breccia (Table 2) – using petrographic context and relative differences in grayscale values of phases expected in lunar samples. Igneous rocks have unique petrographic textures that make them easy to distinguish from other common lunar lithologies, such as breccias (regolith, impact melt, or soil) and impact melts. However, assigning a specific igneous lithological classification is more complicated and requires petrographic intuition and an idea of what minerals comprise the sample. In igneous lunar rocks, the most common phases are air (i.e., vesicles), silica, feldspars, orthopyroxene, Mg-rich olivine, clinopyroxene, oxides (ilmenite and chromite), sulfides, and/or metals in increasing grayscale brightness. Many of these phases have overlapping grayscale values in XCT datasets and can shift depending on specific mineral composition, so assigning specific grayscale values to a mineral phase is not possible. Agglutinates, impact melts, and breccias are a mixture of lunar minerals and lithologies at a wide range of spatial scales, so their classification is dominantly based on textures, not mineralogy.

The classifications and descriptions for the ANGSA Sample Catalog and this paper are not meant to be exhaustive or full petrographic descriptions, but a starting-point for the scientific community to make more informed sample requests for detailed follow-on studies of the XCT data and/or polished sections. We hope that such follow-on studies will utilize the unique perspectives into mineral textures, fabrics, and abundances that XCT data can provide. Below we will briefly describe the nine different lithologic types and their general characteristics. There is significant textural and mineralogical diversity within each of the nine lithologic groups, as well as some obvious sub-groupings, but, for simplicity, we intentionally keep the classifications broad.

546

73001				
Lithology	**# of particles**	**% of particles**	**Mass of particles (g)**	**% of mass**
Agglutinate	1	0.5	0.112	0.1
Anorthosite	4	1.8	0.200	0.2
Basalt, High-Ti	28	12.7	6.736	7.6
Basalt, Low-Ti	3	1.4	0.216	0.2
Granulite	2	0.9	0.194	0.2
Impact Melt	2	0.9	1.528	1.7
Impact Melt Breccia	115	52.3	50.745	56.9
Regolith Breccia	64	29.1	29.360	32.9
Soil Breccia	1	0.5	0.086	0.1
Total	220		89.177	
73002				
Lithology	**# of particles**	**% of particles**	**Mass of particles (g)**	**% of mass**
Agglutinate	6	4.5	0.143	0.3
Anorthosite	0	0.0	0.000	0.0
Basalt, High-Ti	9	6.8	1.639	2.9
Basalt, Low-Ti	4	3.0	0.291	0.5
Granulite	0	0.0	0.000	0.0
Impact Melt	5	3.8	0.247	0.4
Impact-Melt Breccia	42	31.8	18.732	33.1
Regolith Breccia	62	47.0	35.118	62.1
Soil Breccia	4	3.0	0.361	0.6
Total	132		56.531	
Combined				
Lithology	**# of particles**	**% of particles**	**Mass of particles (g)**	**% of mass**
Agglutinate	7	2.0	0.255	0.2
Anorthosite	4	1.1	0.200	0.1
Basalt, High-Ti	37	10.5	8.375	5.7
Basalt, Low-Ti	7	2.0	0.507	0.3
Granulite	2	0.6	0.194	0.1
Impact Melt	7	2.0	1.775	1.2
Impact-Melt Breccia	157	44.6	69.477	47.7
Regolith Breccia	126	35.8	64.478	44.3
Soil Breccia	5	1.4	0.447	0.3
Total	352		145.708	

547

548 **Table 2.** Lithologic classification of >4 mm particles that were scanned from 73001 (n = 220)
549 and 73002 (n = 132).

550

551 ### 3.2.1 “Igneous” fragments

Though few in number, igneous rock fragments are of high scientific interest. The most abundant igneous group are high-Ti basalts, which have igneous textures with a groundmass of intergrown pyroxene and plagioclase (and sometimes olivine) and abundant ilmenite with a range of sizes and shapes (Fig. 7), as well as areas that appear consistent with a vitrophyric groundmass. Low-Ti basalts have igneous textures composed of mostly plagioclase and pyroxene (and sometimes olivine), with lower abundance of ilmenite or other FeTi oxide phases (Fig. 8). Both high-Ti and low-Ti basalts display a large range of crystal sizes and textures. Lunar basalt sub-classification is officially based on Ti concentration (i.e., "high-Ti" has >6 wt. %, "low-Ti" has 1 – 6 wt. %, and "very low-Ti" has <1 wt. %; (Neal & Taylor, 1992; Papike et al., 1976)), but for these samples, they were based on approximate modal abundances of ilmenite. Ilmenite abundances were not quantified but estimated by a visual assessment of the XCT datasets. Basalt particles where ilmenite was a major phase, generally greater than ~8 to 10 vol. %, as determined by the visual assessment, were classified as high-Ti.

Anorthosites are dominated by a low-X-ray-attenuating phase, interpreted to be plagioclase with minor mafic (olivine and/or pyroxene) and trace oxide phases. While these rock fragments are all classified using extrusive igneous rock nomenclature, it is possible that common lunar intrusive igneous lithologies (e.g., troctolites) would be included in these groups, and follow-on petrographic studies of polished sections could provide more accurate classification. Similarly, there are examples in both the low-Ti basalt and anorthosite fragments of samples that are brecciated, but appear to preserve their original igneous lithology with no incorporated regolith or impact melt components (e.g., three of the four anorthosites are brecciated; Fig. 8 i,j).

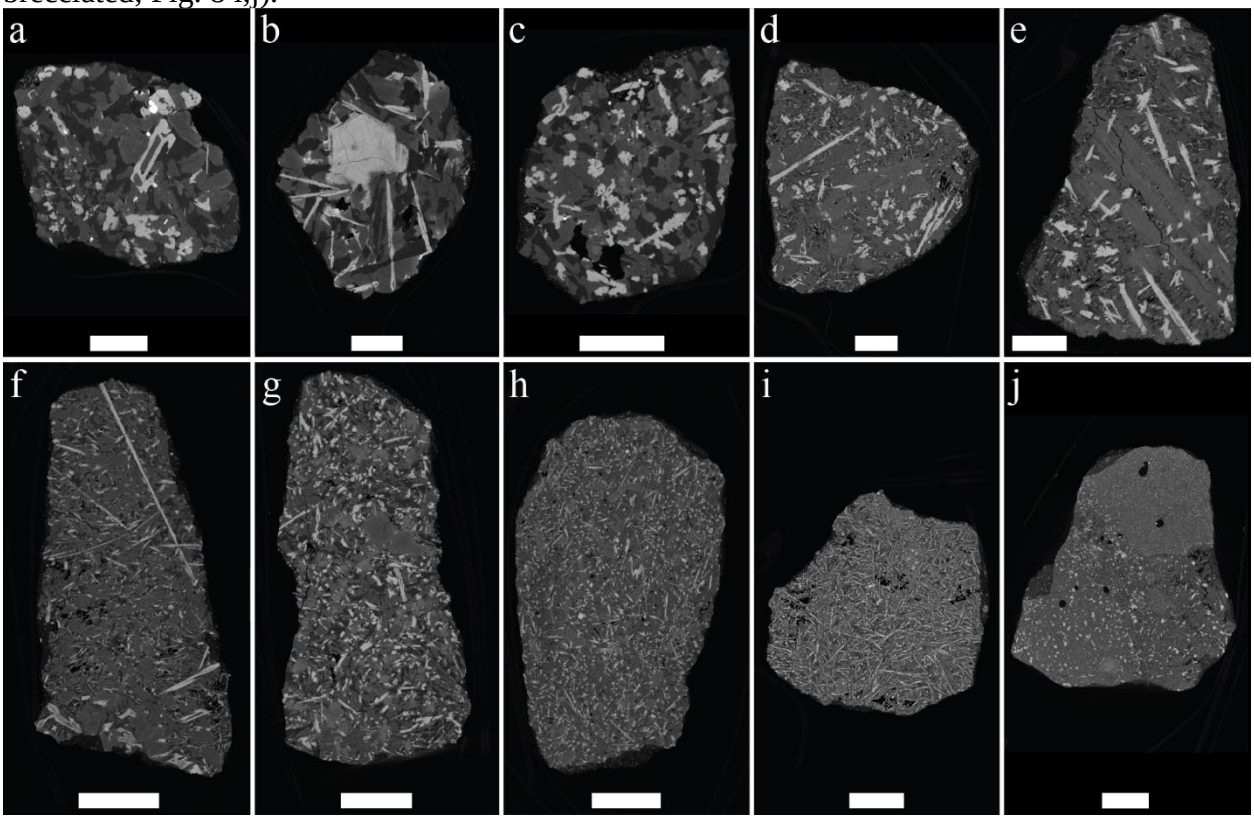

Figure 7. Representative grayscale CT slices of a subset of high-Ti basalts. Groundmass phases are plagioclase (dark gray phase) and mafic phases (pyroxene and possibly olivine; medium gray phase). Ilmenite is the next brighter phase with generally an elongated shape. (j) has three textural domains defined by differences in crystal size and abundance. (a) 73001,125C (b) 73002,1017B (c) 73001,14A (d) 73002,51A (e) 73002,1141A (f) 73001,261(g) 73001,181B (h) 73001,1164A (i) 73001,133 (j) 73001,1183B. All scale bars are 1 mm.

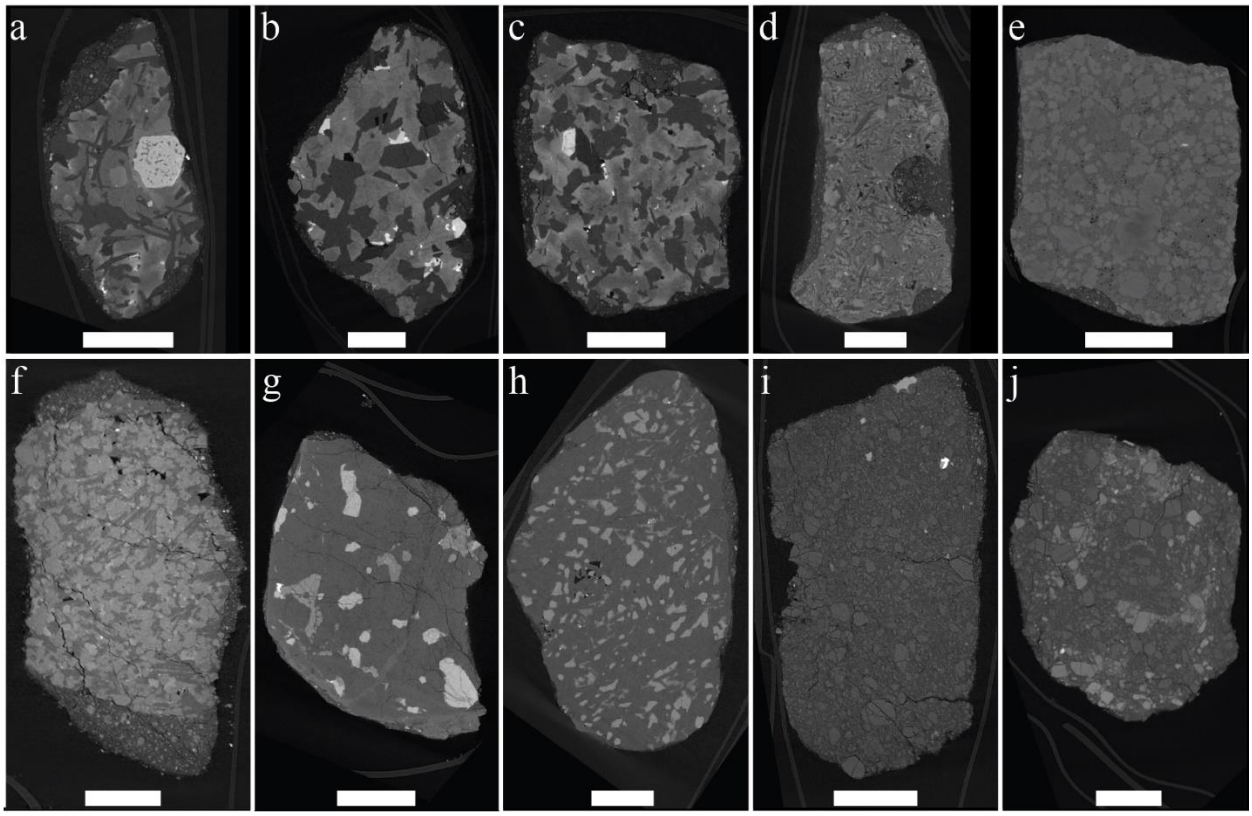

Figure 8. Representative grayscale CT slices of a subset of low-Ti basalts, anorthosites, and granulites. Groundmass phases in the low-Ti basalts (a – f) are plagioclase (dark gray phase) and mafic phases (pyroxene and possibly olivine; medium gray phase). The larger, brighter gray phases are possibly ilmenite or chromite. (g – j) are likely plagioclase (dark groundmass phase), mafic phases (pyroxene and possibly olivine; medium gray phase), and oxides (possibly ilmenite or chromite (brighter gray phase). (a) 73001,18B; low-Ti basalt (b) 73001,1234B; low-Ti basalt (c) 73001,22D; low-Ti basalt (d) 73002,1121C; low-Ti basalt (e) 73002,1017C; low-Ti basalt (f) 73002,1033B; low-Ti basalt (g) 73001,75A; anorthosite (h) 73001,1032A; granulite (i) 73001,1205A; brecciated anorthosite (j) 73002,1121B; brecciated low-Ti basalt. All scale bars are 1 mm.

3.2.2 Regolith fragments

The most abundant type of rock fragment found in the 73001/2 cores are those formed through regolith gardening processes, with low-energy events producing poorly lithified

fragments (i.e., soil breccias), and progressively more energetic events producing more well lithified fragments (i.e., regolith breccias), and even partially or wholly glassy fragments (i.e., agglutinates). The soil breccias observed here are dominantly fine-grained soil with larger mineral and rock clasts that are loosely aggregated (Fig. 9a). These are essentially soil clods but slightly more cohesive than those identified in the whole-core XCT data and thus (partially) survived the dissection, bagging, and scanning processes. Regolith breccias are similar to soil breccias in that they contain abundant rock, glass, and mineral fragments with angular to rounded shapes and a wide variety of compositions, but these are set in a coherent matrix that ranges from clastic to glassy (Fig. 9 b,c). There are numerous regolith breccia particles that were identified to contain interesting lithologies that will be of interest for follow up studies, e.g., basalts, impact or pyroclastic spherules, large metal grains, etc. The agglutinates have a fine-grained, interpreted to be glassy, groundmass with abundant spherical vesicles and smaller rock and mineral fragments, many of which appear to be partially resorbed by the glassy matrix (Fig. 9 d,e). It is possible for regolith breccia fragments to have some agglutinitic glass included within them, and thus the unambiguous identification of an agglutinate, as opposed to an agglutinitic regolith breccia is a judgement call, but the general rule used here is that agglutinates have >40% vesicular glass (by volume).

3.2.3 Impact-melt fragments

The second most abundant type of rock fragment found in the core are those derived from larger impact events, i.e., impact melts, impact breccias, and granulites. These lithologies are thought to be formed through large discrete impact events. The impact melts observed here are generally a single, fine-grained material (interpreted to be glassy material) with sparse bright phases, interpreted to be Fe-metal and fine-grained irregular void spaces (Fig. 9f). They differ from agglutinates in that they do not contain rock and mineral fragments or large, spherical void spaces. Impact-melt breccias are the most diverse of all of the observed groups, but they typically have a glassy to finely crystalline matrix containing lithic and mineral fragments (Fig. 9 g-i). The abundance and diversity of clasts in the impact-melt breccias are both less than what is typically seen in regolith breccias (it is one of the distinguishing characteristics). Many of the impact-melt breccias contain voids, often in abundance, though typically not spherical in shape. There are also abundant metal grains commonly observed in the impact-melt breccias, and these can range in size from tiny specs at the resolution of the scan to several mm’s across. Although the textures observed in the impact-melt breccias are highly variable, there were two subgroups observed within the impact-melt breccias that have similar textures to each other and thus might be petrogenetically related: the poikilitic ilmenite impact melt breccias (n = 29) and the ilmenite lath impact melt breccias (n = 19). Finally, the granulite fragments have three dominant phases, interpreted to be plagioclase and two mafic phases (possibly pyroxene and olivine), and a highly recrystallized texture with rounded crystal boundaries (Figs. 8h and 9j).

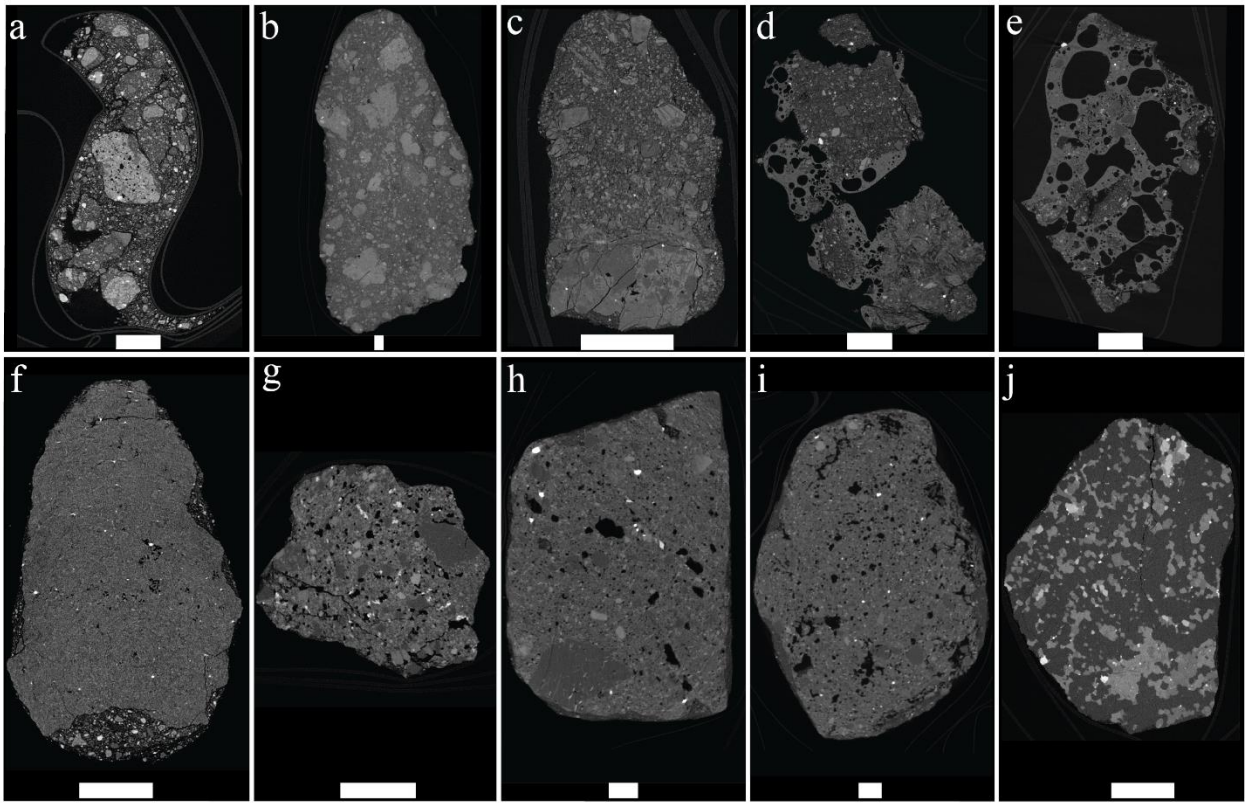

Figure 9. Representative grayscale CT slices of a subset of breccias and other impact-derived lithologies. Due to heterogeneous nature of these samples, mineral and lithic clasts cannot be identified by grayscale brightness. Void spaces are the darkest phase and are easily identified in (d – i). Soil (a) and regolith breccias (b, c) do not have void spaces in the regolith groundmass. (a) 73002,39B; soil breccia (b) 73001,2080; regolith breccia (c) 73001,190B; regolith breccia (d) 73002,1029A; regolith breccia – agglutinitic (e) 73001,1037A; agglutinate (f) 73002,124A; impact-melt breccia (g) 73002,1068A; impact-melt breccia (h) 73002,1132A; impact-melt breccia (i) 73002,2051; impact-melt breccia (j) 72001,209A; granulite. All scale bars are 1 mm.

3.3 Ilmenite Shape Analysis

High-Ti basalts comprise only 10.5% of the removed particles but are some of the most scientifically interesting samples because they reflect the composition and evolution of their mantle sources, track igneous physical and chemical processes, and provide a window into the volatile budget of the lunar interior, among others. Ilmenite within high-Ti basalts is an early-forming mineral whose morphology and size can record the physicochemical evolution of its host melt. Here we present the first 3-D crystal habit measurements of a subpopulation of ilmenite to illustrate the wealth of quantitative insight that can be gained from XCT datasets. This analysis is aided by the fact that ilmenite is a ubiquitous phase within high-Ti basalts and its crystal boundaries are easily distinguishable, unlike other phases, such as feldspars, pyroxene, and olivine.

Three-dimensional analysis of ilmenite crystals from the individually scanned basalt clasts revealed a wide variety of crystal shapes and sizes in different samples and sometimes

within a single sample. We classify crystal shapes using the Sneed and Folk (1958) classification scheme. Of the 350 crystals measured across 14 samples, 60% are very elongated, 14% are very platy, and the rest fall into the other classifications (Table 3; Fig. 10). Table 4 also shows average crystal habit axial lengths (a = longest; b = intermediate; c = shortest) and axial ratios ($\frac{a}{c} : \frac{b}{c}$) for each sample. Average axial ratios are generally anisotropic with a >> b ≈ c for very elongated crystals and a ≈ b >> c in very platy crystals. The supporting information (Text S1; Figs. S9 – S22) contains the following information for each individual sample: Sneed and Folk (1958) ternary diagram and classification statistics, average axial lengths and ratios, and three orthogonal grayscale CT slices outlining a representative crystal. These results indicate that some samples are dominated by a single crystal shape (i.e., 73001,110A; 73001,181B; 73001,261A; 73001,1156A; 73001,1164A; 73002,51A; 73002,1017B; and 73002,1141A; Figs. S9 – S16) whereas others have a range of crystal shapes (i.e., 73001,14A; 73001,125C; 73001,133; 73001,1087A; and 73001,1183B; Figs. S17 – S21) or populations of different crystal shapes (i.e., 73002,80A; Fig. S22). Table S1 contains all crystal measurements.

Shape	No. of crystals	% of crystals
Compact	18	5
Compact-Platy	2	1
Compact-Bladed	17	5
Compact-Elongate	6	2
Platy	6	2
Bladed	11	3
Elongate	9	3
Very-Platy	50	14
Very-Bladed	20	6
Very-Elongate	211	60

Table 3. Number of ilmenite crystals (n = 350) in each (Sneed & Folk, 1958) shape classification across all fourteen measured high-Ti basalt particles.

	Average axial lengths (mm)			Average axial ratios	
Sample	**Longest (a)**	**Intermediate (b)**	**Shortest (c)**	**a/c**	**b/c**
73001, 181B	0.87	0.07	0.05	19.1	1.5
73001, 1164A	0.79	0.07	0.05	17.5	1.5
73001, 14A	0.39	0.20	0.06	6.5	3.4
73001, 133	0.56	0.18	0.02	25.1	8.1
73001, 125C	0.56	0.28	0.09	6.1	3.1
73001, 261A	1.23	0.06	0.04	33.4	1.7
73001, 1183B	0.25	0.11	0.05	5.3	2.3
73001, 1156A	1.22	0.09	0.06	21.3	1.6
73001, 110A	0.79	0.10	0.07	11.6	1.5
73001, 1087A	0.13	0.08	0.07	1.9	1.3
73002, 51A	1.91	0.20	0.13	14.4	1.5

73002, 1141A	2.38	0.23	0.09	25.6	2.5
73002, 1017B	1.07	0.81	0.07	16.0	12.1
73002, 80A	0.41	0.11	0.08	5.4	1.4

675 **Table 4.** Average axial lengths and ratios of ilmenite crystals measured across fourteen high-Ti
676 basalts. 25 crystals were measured per sample.

677

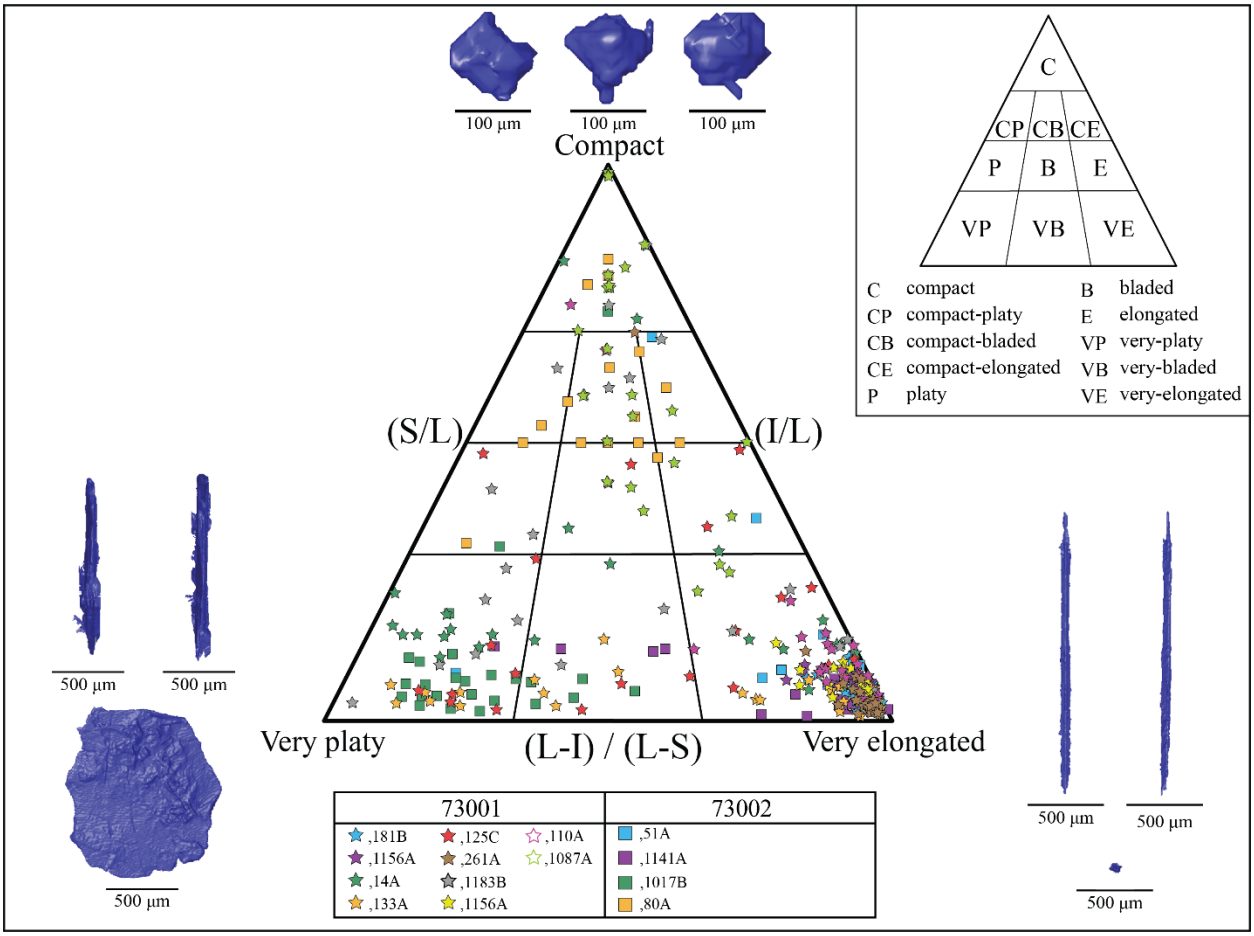

678

679 **Figure 10**. Ilmenite shape classifications. Ternary diagram from the classification scheme of
680 (Sneed & Folk, 1958) showing the shapes of ilmenite crystals (n = 350) measured in fourteen
681 high-Ti basalt particles from 73001 and 73002. Three-dimensional renderings (blue) of crystals
682 are shown from three orthogonal orientations along the long, intermediate, and short crystal habit
683 axes to illustrate end-member crystal shapes.

684

685 We also observe a variety of crystal morphologies that are shown in the orthogonal
686 grayscale images in the supporting information (Figs. S9 – S22). Very elongated crystals
687 generally have sawtooth morphologies characterized by jagged edges and frequently terminate at
688 multiple points, like a pitchfork (e.g., 73001,110A; 73001,181B; Figs. S9 – S10). Some
689 elongated crystals, like in 73001,261A and 73002,51A (Figs. S11 and S14), are zoned with a
690 darker interior and brighter rim, and frequently have a void space in the interior dark material

along the length of the crystal. The interior dark material is interpreted to be armalcolite. Very platy crystals, like in 73002,1017B (Fig. S15), commonly have a euhedral and hexagonal core with small growths emanating from the edges. Crystals with more equant axial ratios commonly show hopper or skeletal external morphologies, characterized by reentrant growth features (e.g., 73001,14A; 73001,125C; 73001,1087A and 73002,80A; Figs. S17, S18, S20, and S22, respectively).

While a more detailed analysis of crystal size and spatial distributions is needed, we do see different apparent crystal size and spatial distributions. For instance, 73001,261A (Fig. S11) shows two populations of ilmenite crystals, one that is coarse and zoned and the other that is fine-grained and acicular, that are spatially separated. Sample 73001,1183B (Fig. S21) has three distinct lithologies with different crystal sizes, shapes, and abundances. We frequently see samples with large, very elongated crystals with random spatial distributions juxtaposed to domains of finer-grained mesostasis that have much smaller ilmenite crystals (e.g., 73001,110A; 73001,261A; 73001,1156A; 73002,51A; and 73002,1141A; Figs. S9, S11, S12, S14, and S16, respectively). Some samples have a single population of crystals with an apparently linear crystal size distribution and uniform spatial distribution (e.g., 73002,1017B; 73001,133; 73001,1087A; 73002,80A; Figs. S15, S19, S20, and S22, respectively).

4 Discussion

4.1 Utility of XCT for 73001 and 73002 characterization

X-ray computed tomography scanning of the entire lengths of 73001 and 73002 has provided a permanent record of the relatively undisturbed stratigraphy of the core material before it was necessarily disturbed by the extrusion/dissection process. This dataset is the only intact 3-D archive of lunar stratigraphy up to 70 cm depth and can provide a wealth of scientific and engineering information, such as the dynamics of lunar mass wasting events (Magnarini et al., this issue), regolith gardening from micrometeoroid impacts (McFadden et al., 2024), and density and other physical properties of lunar soil, as well as providing a stratigraphic 3-D context for placing other datasets, such as maturity, reflectance, geochemistry, and the continuous thin sections (Bell et al., 2024; Neuman et al., this issue; Neuman et al., 2025; Simon et al., 2024).

In addition to the scientific and engineering utility, these datasets proved to be invaluable during the extrusion and dissection processes (Gross et al., this issue). Sample processors were able to orient the core in a way that prevented slumping during extrusion due to large void spaces in 73002. They were also able to use the data to inform what clasts were to be expected during each dissection pass. Had large angular rock fragments been observed near the margins of the drive tube, special care during extrusion would have been taken to ensure that these fragments did not foul the extrusion process. Finally, the observation that the “keeper” at the top of the 73001 drive tube was not seated properly inside the tube, and thus the regolith inside the tube would not have been properly immobilized if it was removed from the CSVC, was vitally important information. The procedure for transporting and XCT scanning the whole tube, as well as the procedure for extruding the core had to be modified in order to not significantly disturb the stratigraphy of the sample.

Upon dissection and removal of the >4 mm particles from the core, most were coated in fine-grained lunar soil, obfuscating their lithologic classification through visible assessment in

the pristine lunar curation environment. By individually XCT scanning these particles in a way that keeps the samples pristine, we were able to confidently classify most samples, and identify potentially new lunar lithologies, while still maintaining their pristine nature. Furthermore, the XCT data proved to be a valuable guide to selecting representative clasts for more destructive non-pristine thin sectioning. Without the XCT data, we would have needed to make more of the dust-coated clasts non-pristine to reach the same level of representativeness among the polished sections of clasts from 73001 and 73002. The XCT scans were also beneficial in helping intentionally select particles for other follow-on studies, including targeted sectioning and subsampling of unique clasts or features (Shearer et al., this issue). Finally, the XCT data provided valuable, and sometimes the only, petrologic context for some clasts that were allocated for destructive bulk rock analyses (Cohen et al., this issue).

Because the depth of each individually-scanned particle was well documented, we are able to assess lithologic variation with depth. For example, regolith fragments are much more common at shallower depths (i.e., 62% regolith breccias by mass in 73002) than at greater depths (33% regolith breccias by mass in 73001), which is consistent with the production of these through impact gardening of the local regolith materials. This trend was also documented in the <1 mm soil size fractions removed from 73002 and analyzed by scanning electron microscopy (Simon et al., 2024). Conversely, impact melt breccias are much more common at greater depths, 57% by mass in 73001, compared to 33% in 73002. Similarly, there is an increase in the amount of basaltic material at depth in 73001 (7.8% by mass) versus what is observed in the shallower 73002 material (3.4% by mass). Although it is dangerous to overinterpret the implications of these depth dependencies for just the >4 mm material, because of the relatively small number of particles, if this classification scheme is extended to smaller particles (e.g., 1-4 mm particles in the whole core scans), then constraints on the provenances of the materials included in this landslide deposit might be possible.

4.2 High-Ti basalt clasts from various physicochemical environments

The size and morphology of ilmenite in high-Ti basalt clasts reflects the thermodynamic conditions of the host melt. Usselman (1975) showed experimentally that ilmenite morphology varies as a function of cooling rate. Morphologies vary from dendritic to acicular to tabular with decreased cooling rate. Donohue and Neal (2015) (and references therein) provide a recent review of lunar ilmenite morphologies and 2-D analysis of a comprehensive set of Apollo 17 basalt morphologies and crystal size distributions. Our 3-D analysis of lunar ilmenite corroborates their findings, showing that a wide range of ilmenite morphologies exist and that 73001 and 73002 contain basalt clasts that represent various physicochemical conditions. Valenciano et al., (this issue) conducted augmented 2-D ilmenite crystal size distribution (CSD) analyses using XCT slices for several high-Ti basalt particles from 73002. Their results confirm that 73002 contains basaltic material from several flows.

We also find that 2-D CSD analysis of lunar ilmenite using the *CSDSlice* program (Morgan & Jerram, 2006), which is commonly used to stereologically predict 3-D shapes from 2-D measurements, underestimates the axial ratios for very elongated crystals; Donohue and Neal (2015) report ilmenite maximum axial ratios of 10:1, while our 3-D results are 2-3x higher (Table 4). Samples that have many very platy crystals (e.g., 73002,1017B) are also likely to be misrepresented using stereological conversions of 2-D measurements since any crystal that is not oriented parallel to the thin section will have a bladed to elongated apparent shape. Measuring

the shape of every crystal in 3-D to provide a CSD that does not require stereological conversions would be ideal, but is currently not feasible given the number of crystals and their intergrown nature. However, the augmented 2-D CSD methods by Valenciano et al., (this issue) produced axial ratios more comparable to what we measured. We hope that the ilmenite measurements provided here can supplement stereological predictions in future CSD analyses performed in 2-D.

5 Conclusions

X-ray computed tomography was crucial for the preliminary examination of Apollo drive tubes 73001 and 73002. Whole-core scans aided in the opening, extrusion, and dissection of 73001 and 73002. They also provide a high-resolution 3-D archive of lunar soil that can be used by future researchers to better understand the dynamics of lunar landslides, regolith gardening processes, and the physical nature of the lunar subsurface up to 70 cm depth. Individual scans of the 352 >4 mm particles were critical for their classification, providing 3-D context and guidance for subsequent chipping and sectioning, and will also allow future researchers the opportunity to understand the textures, abundances, crystal morphologies, fabrics, and mineralogy of a large variety of lunar lithologies. We provide an example of how the XCT data for fourteen high-Ti basalt clasts can be used to better constrain the shape and morphology of lunar ilmenite, and use these results to show that high-Ti basalt clasts from 73001 and 73002 experienced a range of physicochemical conditions.

Continued work in advanced curation research will evaluate XCT as a PE tool (McCubbin et al., 2019). For future analysis of astromaterials, the benefits of XCT scanning need to be weighed against the potential negative effects such as eradication of thermoluminescence signals or potential alteration of organic material, and whether the information lost from those techniques can be wholly or partially mitigated using other techniques (e.g., cosmogenic nuclide studies). Many current and future sample return missions have or plan to implement XCT for preliminary examination (Fukai et al., 2024; Gross et al., this issue; Righter et al., 2023; Tait et al., 2022), illustrating the usefulness of these data for the curation processors and the general scientific community.

Acknowledgments

We thank the curation staff within the Astromaterials Research and Exploration Science (ARES) Division at NASA Johnson Space Center and all members of the ANGSA Science Team. This work was supported through NASA Apollo Next Generation Sample Analysis (ANGSA) grant 80NSSC19K0958. UTCT acknowledges support from the NASA Planetary Science Enabling Facility program (award 80NSSC23K0199) and the NSF EAR-IF Community Facility program (award EAR-2223808). We thank the two anonymous reviewers and the editor Amanda Hendrix for their comments and suggestions that helped improve this manuscript.

Open Research

Additional details are reported in Supporting Information S1. Large files (Tables S1 and S2; Movies S1 and S2) are stored in a Mendeley Data Repository (Eckley, 2025). All XCT datasets are publicly available from the AstroMat Data System (Eckley et al., 2024b). DOIs for each individual dataset are found in Table S2.

References

Bell, S. K., Joy, K. H., Nottingham, M., Tartèse, R., Jones, R. H., Kent, J. J., Shearer, C. K., & the ANGSA Science Team. (2024). Automated mineralogy analysis of the Apollo 17 73002 continuous core thin sections using QEMSCAN mapping techniques, *Journal of Geophysical Research: Planets*, *129*(12), e2024JE008359.

Cnudde, V., & Boone, M. N. (2013). High-resolution X-ray computed tomography in geosciences: A review of the current technology and applications, *Earth-Science Reviews*, *123*, 1-17.

Cohen, B. A., Curran, N. M., Valencia, S. N., Bullock, E. S., Corrigan, C. M., Alevy, E. G., Eckley, S. A., & the ANGSA Science Team. (2024). Composition, Mineralogy, and Noble-Gas Content of Apollo 17 Particles and Soils from the 73002 Drive Tube. *Journal of Geophysical Research: Planets* (this issue).

Donohue, P. H., & Neal, C. R. (2015). Quantitative textural analysis of ilmenite in Apollo 17 high-titanium mare basalts, *Geochimica et Cosmochimica Acta*, *149*, 115-130.

Eckley, S. A. (2025). Large supporting files for ANGSA X-ray CT paper [Dataset]. Mendeley Data. V.1, doi:10.17632/5y725j47wf.1.

Eckley, S. A., Ketcham, R. A., Liu, Y., Gross, J., & McCubbin, F. M. (2024a). Emplacement of shergottites in the Martian crust inferred from three-dimensional petrofabric and crystal size distribution analyses, *Meteoritics & Planetary Science*, *59*(7), 1523-1545.

Eckley, S. A., Zeigler, R. A., Ketcham, R. A., Edey, D., Hanna, R. D., & Gross, J. (2024b). 73001 and 73002 XCT Collection - ANGSA. Version 1.0, [Dataset]. Astromaterials Data Archive, doi:https://doi.org/10.60707/9zf3-h517.

Friedrich, J. M., McLain, H. L., Dworkin, J. P., Glavin, D. P., Towbin, W. H., Hill, M., & Ebel, D. S. (2019). Effect of polychromatic X-ray microtomography imaging on the amino acid content of the Murchison CM chondrite, *Meteoritics & Planetary Science*, *54*(1), 220-228.

Fukai, R., Usui, T., Fujiya, W., Takano, Y., Bajo, K. i., Beck, A., Bonato, E., Chabot, N. L., Furukawa, Y., & Genda, H. (2024). Curation protocol of Phobos sample returned by Martian Moons eXploration, *Meteoritics & Planetary Science*, *59*(2), 321-337.

Gawronska, A. J., McLeod, C. L., Blumenfeld, E. H., Hanna, R. D., & Zeigler, R. A. (2022). New interpretations of lunar mare basalt flow emplacement from XCT analysis of Apollo samples, *Icarus*, *388*, 115216.

Glavin, D. P., Eckley, S. A., Aponte, J. C., Berger, E. L., Burton, A. S., Dworkin, J. P., Elsila, J. E., Ferguson, F. T., Furukawa, Y., & Graham, H. V. (2024). Investigating the impact of x-ray computed tomography imaging on soluble organic matter in the Murchison meteorite: Implications for Bennu sample analyses, *Meteoritics & Planetary Science*, *59*(1), 105-133.

Goguen, J., Sharits, A., Chiaramonti, A., Lafarge, T., & Garboczi, E. (2024). Three-dimensional characterization of particle size, shape, and internal porosity for Apollo 11 and Apollo 14 lunar regolith and JSC-1A lunar regolith soil simulant, *Icarus*, 116166.

Gross, J., Mosie, A. B., Krysher, C., Zeigler, R. A., Eckley, S. A., Ketcham, R. A., Hanna, R. D., Edey, D., Kent, J. J., McCubbin, F. M., McDonald, F., Schild, T., Lucey, P. G., Sun, L., Flom, A., Petro, N. E., Shearer, C. K., & the ANGSA Science Team. (2024). Apollo Next Generation Sample Analysis (ANGSA) samples: Preliminary examination of double

drive tube samples 73001 and 73002 and lessons learned for returning to the Moon with Artemis. *Journal of Geophysical Research: Planets* (this issue).

Hanna, R. D., & Ketcham, R. A. (2017). X-ray computed tomography of planetary materials: A primer and review of recent studies, *Chemie der Erde-Geochemistry*, *77*(4), 547-572.

Huang, T. J., Ganju, E., Torbatisarraf, H., Thompson, M. S., & Chawla, N. (2024). Advanced microstructural and compositional analysis of a lunar agglutinate from the Apollo 11 mission, *Meteoritics & Planetary Science*, *59*(6), 1455-1472.

Katagiri, J., Matsushima, T., Yamada, Y., Tsuchiyama, A., Nakano, T., Uesugi, K., Ohtake, M., & Saiki, K. (2015). Investigation of 3D grain shape characteristics of lunar soil retrieved in Apollo 16 using image-based discrete-element modeling, *Journal of Aerospace Engineering*, *28*(4), 04014092.

Ketcham, R. A. (2006). New algorithms for ring artifact removal, paper presented at Developments in X-ray tomography V, SPIE.

Ketcham, R. A., & Carlson, W. D. (2001). Acquisition, optimization and interpretation of X-ray computed tomographic imagery: applications to the geosciences, *Computers & Geosciences*, *27*(4), 381-400.

Lowe, D. G. (2004). Distinctive image features from scale-invariant keypoints, *International journal of computer vision*, *60*, 91-110.

Magnarini, G., Mitchell, T. M., Grindrod, P. M., Bell, S. K., Joy, K. H., Eckley, S. A., Zeigler, R. A., Schmitt, H. H., Shearer, C. K., & the ANGSA Science Team. (2024). 3D and 2D clast analysis of Apollo 17 core sample 73002: insights into the Light Mantle dynamics and regolith reworking. *Journal of Geophysical Research: Planets* (this issue).

McCubbin, F. M., Herd, C. D., Yada, T., Hutzler, A., Calaway, M. J., Allton, J. H., Corrigan, C. M., Fries, M. D., Harrington, A. D., & McCoy, T. J. (2019). Advanced curation of astromaterials for planetary science, *Space Science Reviews*, *215*, 1-81.

McFadden, J. A., Thompson, M. S., Keller, L. P., Christoffersen, R., Morris, R. V., Shearer, C., & the ANGSA Science Team. (2024). Analyzing the mineralogy and space weathering characteristics of the finest fraction in Apollo core sample 73002, *Journal of Geophysical Research: Planets*, *129*(11), e2024JE008528.

Morgan, D. J., & Jerram, D. A. (2006). On estimating crystal shape for crystal size distribution analysis, *Journal of Volcanology and Geothermal Research*, *154*(1-2), 1-7.

Neal, C. R., & Taylor, L. A. (1992). Petrogenesis of mare basalts: A record of lunar volcanism, *Geochimica et Cosmochimica Acta*, *56*(6), 2177-2211.

Neuman, M., Jolliff, B. L., Wang, K., Petro, N., Valenciano, J., Neal, C. R., Eckley, S. A., Kent, J., Sun, L., Lucey, P., Bell, S., Joy, K. H., Tartese, R., Jones, R., Carpenter, P., Morris, R. V., Haney, N. C., Simon, S. B., Cato, M., Shearer, C. K., Welten, K. C., Nishiizumi, K., Caffee, M. W., Colina-Ruiz, R. A., Kroll, T., Sokaras, D., Ishii, H. A., Bradley, J. P., Gillis-Davis, J., McFadden, J. A., Thompson, M. S., Christoffersen, R., Keller, L. P., Simon, J. I., McCubbin, F. M., Zeigler, R. A., Gross, J., Ketcham, R. A., Hanna, R. D., Edey, D., & the ANGSA Science Team. (2025). Revealing the Moon's Taurus-Littrow Landslide via Integrated Analysis of Pristine Apollo 17 Soil Core 73001/2. *Journal of Geophysical Research: Planets* (this issue).

Neuman, M., Koefoed, P., Wang, K., Jolliff, B. L., Korotev, R. L., & Morris, R. V. (2025). Major and trace element variations and lithologic component analysis in Apollo 17 drive tube 73001/2, *Journal of Geophysical Research: Planets*, *130*(1), e2024JE008373.

Papike, J. J., Hodges, F. N., Bence, A., Cameron, M., & Rhodes, J. (1976). Mare basalts: Crystal chemistry, mineralogy, and petrology, *Reviews of Geophysics*, *14*(4), 475-540.

Righter, K., Lunning, N. G., Nakamura-Messenger, K., Snead, C. J., McQuillan, J., Calaway, M., Allums, K., Rodriguez, M., Funk, R. C., & Harrington, R. S. (2023). Curation planning and facilities for asteroid Bennu samples returned by the OSIRIS-RE x mission, *Meteoritics & Planetary Science*, *58*(4), 572-590.

Schneider, C. A., Rasband, W. S., & Eliceiri, K. W. (2012). NIH Image to ImageJ: 25 years of image analysis, *Nature methods*, *9*(7), 671-675.

Sears, D. W., Sears, H., Ebel, D. S., Wallace, S., & Friedrich, J. M. (2016). X-ray computed tomography imaging: A not-so-nondestructive technique, *Meteoritics & Planetary Science*, *51*(4), 833-838.

Sears, D. W., Sehlke, A., Friedrich, J. M., Rivers, M. L., & Ebel, D. S. (2018). X-ray computed tomography of extraterrestrial rocks eradicates their natural radiation record and the information it contains, *Meteoritics & Planetary Science*, *53*(12), 2624-2631.

Shearer, C. K., McCubbin, F. M., Eckley, S. A., Simon, S. B., Meshik, A., McDonald, F., Schmitt, H. H., Zeigler, R. A., Gross, J., & Mitchell, J. (2024). Apollo Next Generation Sample Analysis (ANGSA): An Apollo participating scientist program to prepare the lunar sample community for Artemis, *Space Science Reviews*, *220*(6), 62.

Shearer, C. K., Simon, S. B., Erickson, T. M., Neal, C. R., Valenciano, J. L., Simon, J. I., Eckley, S. A., Jolliff, B. L., Moriarty, D. P., & the ANGSA Science Team. (2025). High-Ti Melts from the Taurus-Littrow Valley (TLV). A Product of Volcanism or Impact? An ANGSA Investigation Using the Station 3 Double Drive Tube 73001-73002. *Journal of Geophysical Research: Planets* (this issue).

Simon, S. B., Cato, M. J., Shearer, C. K., & Team, A. S. (2024). Modal petrology and mineral chemistry of the< 1 mm size fraction of lunar regolith in Apollo 17 drive tube section 73002, *Journal of Geophysical Research: Planets*, *129*(1), e2023JE007991.

Sneed, E. D., & Folk, R. L. (1958). Pebbles in the lower Colorado River, Texas a study in particle morphogenesis, *The Journal of geology*, *66*(2), 114-150.

Tait, K. T., McCubbin, F. M., Smith, C. L., Agee, C. B., Busemann, H., Cavalazzi, B., Debaille, V., Hutzler, A., Usui, T., & Kminek, G. (2022). Preliminary planning for mars sample return (MSR) curation activities in a sample receiving facility (SRF), *Astrobiology*, *22*(S1), S-57-S-80.

Tsuchiyama, A., Sakurama, T., Nakano, T., Uesugi, K., Ohtake, M., Matsushima, T., Terakado, K., & Galimov, E. M. (2022). Three-dimensional shape distribution of lunar regolith particles collected by the Apollo and Luna programs, *Earth, Planets and Space*, *74*(1), 172.

Usselman, T. (1975). Ilmenite chemistry in mare basalts, an experimental study, paper presented at *Origins of Mare Basalts and their Implications for Lunar Evolution*.

Valenciano, J., Neal, C. R., Eckley, S. A., & Shearer, C. K. (2024). An ANGSA Study: Crystal Size Distribution of Ilmenite in Basalts from Apollo 17 Drive Tube 73002. *Journal of Geophysical Research: Planets* (this issue).

Wilbur, Z. E., Barnes, J. J., Eckley, S. A., Erickson, T. M., Zeigler, R. A., & Domanik, K. (2025). Evaluating the crystallization and eruptive histories of low-titanium basalts with 2D and 3D studies, *Geochimica et Cosmochimica Acta*, *389*, 110-124.

Wilbur, Z. E., Barnes, J. J., Eckley, S. A., Ong, I. J., Brounce, M., Crow, C. A., Erickson, T. M., Kent, J. J., Boyce, J. W., & Mosenfelder, J. L. (2023). Volatiles, vesicles, and vugs:

Unraveling the magmatic and eruptive histories of Steno crater basalts, *Meteoritics & Planetary Science*, *58*(11), 1600-1628.

Wilkerson, R. P., Rickman, D. L., McElderry, J. R., Walker, S. R., & Cannon, K. M. (2024). On the measurement of shape: With applications to lunar regolith, *Icarus*, *412*, 115963.

Withers, P. J., Bouman, C., Carmignato, S., Cnudde, V., Grimaldi, D., Hagen, C. K., Maire, E., Manley, M., Du Plessis, A., & Stock, S. R. (2021). X-ray computed tomography, *Nature Reviews Methods Primers*, *1*(1), 18.

Appendix A: The ANGSA Science Team

Name	**Email Address**	**Affiliation**
Caitlin Ahrens	Caitlin.ahrens@nasa.gov	NASA Goddard Space Flight Center
Judith Allton	Judith.h.allton@nasa.gov	NASA Johnson Space Center
Cecilia Amick	cecilia.l.amick@nasa.gov	Jacobs NASA Johnson Space Center
Mahesh Anand	mahesh.anand@open.ac.uk	Open University
Benoit Andre	Benoit.andre@esa.int	European Space Agency
Jose Aponte	jose.c.aponte@nasa.gov	NASA Goddard Space Flight Center
Matteo Appolloni	Matteo.appolloni@esa.int	European Space Agency
Nathan Bamsey	Nathan.bamsey@esa.int	European Space Agency
Jessica Barnes	jjbarnes@lpl.arizona.edu	University of Arizona
Samantha Bell	samantha.bell@manchester.ac.uk	University of Manchester
Riccardo Biella	Riccardo.biella@esa.int	European Space Agency
Lars Borg	borg5@llnl.gov	Lawrence Livermore National Laboratory
Jeremy Boyce	jeremy.w.boyce@nasa.gov	NASA Johnson Space Center
John Bradley	johnbrad@hawaii.edu	University of Hawaii
Alex Bradley	abradley@eps.wustl.edu	Washington University St. Louis
Adrian Brearley	brearley@unm.edu	University of New Mexico
Maryjo Brounce	mbrounce@ucr.edu	University of California Riverside
Emma Bullock	ebullock@carnegiescience.edu	Carnegie Earth and Planets Laboratory
Kate Burgess	kate.burgess@nrl.navy.mil	Naval Research Laboratory
Yuriy Butenko	Yuriy.butenko@esa.int	European Space Agency
Marc Caffee	mcaffee@purdue.edu	Purdue University
Erick Cano	ejcano@unm.edu	University of New Mexico
James Carpenter	james.carpenter@esa.int	European Space Agency
Paul Carpenter	Paulc@levee.wustl.edu	Washington University St. Louis
Gianluca Casarosa	Gianluca.casarosa@esa.int	European Space Agency
William Cassata	wcassata@bgc.org	Berkeley Geochronology Center
Michael Cato	mcato@unm.edu	University of New Mexico
Simon Clemett	simon.j.clemett@nasa.gov	Jacobs NASA Johnson Space Center
Barbara Cohen	barbara.a.cohen@nasa.gov	NASA Goddard Space Flight Center
Roberto Colina-Ruiz	rcolina@stanford.edu	SLAC National Accelerator Laboratory
Catherine Corrigan	corriganc@si.edu	National Museum of Natural History
Aidan Cowley	aidan.cowley@esa.int;	European Space Agency

Cyrille Crespi	Cyrille.crespi@esa.int	European Space Agency
Roy Cristofferson	roy.christoffersen-1@nasa.gov	Jacobs NASA Johnson Space Center
Carolyn Crow	carolyn.crow@colorado.edu	University of Colorado Boulder
Natalie Curran	natalie.m.curran@nasa.gov	NASA Goddard Space Flight Center
Brittany Cymes	brittany.cymes.ctr@nrl.navy.mil	Naval Research Laboratory
Paul deMediros	Paul.demediros@esa.int	European Space Agency
James Dottin	James_dottin@brown.edu	Brown University
Catherine Dukes	cdukes@virginia.edu	University of Virginia
Jason Dworkin	Jason.p.dworkin@nasa.gov	NASA Goddard Space Flight Center
Darby Dyar	mdyar@mtholyoke.edu	Mount Holyoke College/PSI
Scott Eckley	scott.a.eckley@nasa.gov	Jacobs NASA Johnson Space Center
David Edey	dave.edey@utexas.edu	University of Texas, Austin
Jamie Elsila	jamie.e.cook@nasa.gov	NASA Goddard Space Flight Center
Timmons Erickson	Timmons.m.erickson@nasa.gov	Jacobs NASA Johnson Space Center
Chiara Ferrari-Wong	cfw@hawaii.edu	University of Hawaii
Abbey Flom	aflom@hawaii.edu	University of Hawaii
Kate Freeman	khf4@psu.edu	Penn State University
Amy Gaffney	gaffney1@llnl.gov	Lawrence Livermore National Laboratory
Lauren Galien	lgalien@nd.edu	University of Notre Dame
Anthony Gargano	agargano@unm.edu	University of New Mexico
Jeffrey Gillis-Davis	j.gillis-davis@wustl.edu	Washington University St. Louis
Daniel Glavin	Daniel.p.glavin@nasa.gov	NASA Goddard Space Flight Center
Peter Grindrod	p.grindrod@nhm.ac.uk	Natural History Museum London
Juliane Gross	juliane.gross@nasa.gov	NASA Johnson Space Center
Timothy Hahn	timothy.m.hahn@nasa.gov	Jacobs NASA Johnson Space Center
Romy Hanna	romy@jsg.utexas.edu	University of Texas, Austin
Tin Ho	Thh8pue@virginia.edu	University of Virginia
Hope Ishii	ishii3@hawaii.edu	University of Hawaii
Bradley Jolliff	bjolliff@wustl.edu	Washington University St. Louis
Rhian Jones	rhian.jones-2@manchester.ac.uk	University of Manchester
Katherine Joy	Katherine.joy@manchester.ac.uk	University of Manchester
Lindsay Keller	lindsay.p.keller@nasa.gov	NASA Johnson Space Center
Jeremy Kent	jeremy.j.kent@nasa.gov	GeoControl NASA Johnson Space Center
Richard Ketcham	ketcham@jsg.utexas.edu	University of Texas, Austin
Grant Killian	Gk3uk@virginia.edu	University of Virginia
Corliss Kin Sio	sio2@llnl.gov	Lawrence Livermore National Laboratory
Randy Korotev	korotev@wustl.edu	Washington University St. Louis
Thomas Kroll	tkroll@slac.stanford.edu	SLAC National Accelerator Laboratory
Thomas Kruijer	kruijer1@llnl.gov	Lawrence Livermore National Laboratory
Charis Krysher	charis.h.krysher@nasa.gov	Jacobs NASA Johnson Space Center
Antonio Lanzirotti	lanzirotti@uchicago.edu	University of Chicago
Ernest Lewis	ernest.k.lewis@nasa.gov	Jacobs NASA Johnson Space Center
Robert Linder	Robert.lindner@esa.int	European Space Agency

Gordon Love	glove@ucr.edu	University of California Riverside
Paul Lucey	lucey@higp.hawaii.edu	University of Hawaii
Giulia Magnarini	Giulia.magnarini.14@ucl.ac.uk	University College, London
Advenit Makaya	Advenit.makaya@esa.int	European Space Agency
Dayl Martin	dayl.martin@esa.int	European Space Agency
Matthias Maurer	Matthias.Maurer@esa.int;	European Space Agency
Jillian Maxson	jtm8hqg@virginia.edu	University of Virginia
Molly McCanta	mmccanta@utk.edu	University of Tennessee, Knoxville
Francis McCubbin	francis.m.mccubbin@nasa.gov	NASA Johnson Space Center
Francesca McDonald	Francesca.mcdonald@esa.int	European Space Agency
James McFadden	mcfadde8@purdue.edu	Purdue University
Hannah McLain	Hannah.I.mclain@nasa.gov	NASA Goddard Space Flight Center
Alex Meshik	ameshik@physics.wustl.edu	Washington University St. Louis
Alexandre Meurisse	Alexandre.Meurisse@esa.int	European Space Agency
Grace Minesinger	gmm9uf@virginia.edu	University of Virginia
Angelina Minocha	angelinam@wustl.edu	Washington University St. Louis
Julie Mitchell	julie.l.mitchell@nasa.gov	NASA Johnson Space Center
Thomas Mitchell	tom.mitchell@ucl.ac.uk	University College, London
Dan Moriarty	daniel.p.moriarty@nasa.gov	NASA Goddard Space Flight Center
Richard Morris	richard.v.morris@nasa.gov	NASA Johnson Space Center
Jed Mosenfelder	jmosenfe@umn.edu	University of Minnesota
Andrea Mosie	andrea.b.mosie@nasa.gov	Jacobs NASA Johnson Space Center
Clive Neal	cneal@nd.edu	University of Notre Dame
Mason Neuman	mdneuman@wustl.edu	Washington University St. Louis
Kunihiko Nishizumi	kuni@berkeley.edu	University of California Berkeley
Ryan Ogliore	rogliore@wustl.edu	Washington University St. Louis
Evan O'Neal	evan.w.o'neal@nasa.gov	Jacobs NASA Johnson Space Center
Iunn Jenn Ong	oij4869@email.arizona.edu	University of Arizona
Jessica Oraegbu	mfg9rv@virginia.edu	University of Virginia
James Papike	jpapike@unm.edu	University of New Mexico
Rita Parai	parai@wustl.edu	Washington University St. Louis
Noah Petro	noah.e.petro@nasa.gov	NASA Goddard Space Flight Center
Sean Pomeroy	Sean.Pomeroy@colorado.edu	University of Colorado Boulder
Olga Pravdivtseva	olga@wustl.edu	Washington University St. Louis
Kelsey Prissel	Kelsey.prissel@nasa.gov	Jacobs NASA Johnson Space Center
Tabb Prissel	tabb.c.prissel@nasa.gov	NASA Johnson Space Center
Julian Rodriguez	smrodriguez@wustl.edu	Washington University St. Louis
Thomas Rohr	Thomas.rohr@esa.int	European Space Agency
Timon Schild	Timon.schild@esa.int	European Space Agency
Harrison Schmitt	hhschmitt@earthlink.net	Harrison Schmitt Consulting
Derek Sears	derekwgsears@gmail.com	NASA AMES Research Center
Alexander Sehlke	alexander.sehlke@nasa.gov	NASA AMES Research Center
Zachary Sharp	zsharp@unm.edu	University of New Mexico

Charles Shearer	cshearer@unm.edu	University of New Mexico
Danielle Simkus	Danielle.n.simkus@nasa.gov	NASA Goddard Space Flight Center
Justin Simon	justin.i.simon@nasa.gov	NASA Johnson Space Center
Steven Simon	sbs8@unm.edu	University of New Mexico
Elizabeth Sklute	ecsklute@psi.edu	Planetary Science Institute
Dimosthenis Sokaras	dsokaras@slac.stanford.edu	SLAC National Accelerator Laboratory
Kamil Stelmach	kbs7dqw@virginia.edu	University of Virginia
Rhonda Stroud	stroud@nrl.navy.mil	Naval Research Laboratory
Lingzhi Sun	lzsun@higp.hawaii.edu	University of Hawaii
Stephen Sutton	sutton@cars.uchicago.edu	University of Chicago
Romain Tartese	romain.tartese@manchester.ac.uk	University of Manchester
Fiona Thiessen	Fiona.thiessen@esa.int	European Space Agency
Kathie Thomas-Keprta	kathie.thomas-keprta-1@nasa.gov	Jacobs NASA Johnson Space Center
Michelle Thompson	thomp655@purdue.edu	Purdue University
Zhen Tian	t.zhen@wustl.edu	Washington University St. Louis
Eoin Tuohy	Eoin.tuohy@esa.int	European Space Agency
Sarah Valencia	sarah.n.valencia@nasa.gov	University of Maryland
Jessika Valenciano	Jvalenc2@nd.edu	University of Notre Dame
Richard Walker	rjwalker@umd.edu	University of Maryland
Richard Walroth	rwalroth@stanford.edu	SLAC National Accelerator Laboratory
Kun Wang	wangkun@wustl.edu	Washington University St. Louis
Stu Webb	gwebb1@nd.edu	University of Notre Dame
Kees Welten	kcwelten@berkeley.edu	University of California Berkeley
Zoe Wilbur	zewilbur@email.arizona.edu	University of Arizona
Patrizia Will	Patrizia.will@wustl.edu	Washington University St. Louis
Josh Wimpenny	wimpenny1@llnl.gov	Lawrence Livermore National Laboratory
Adam Woodson	akw8r@virginia.edu	University of Virginia
Chris Yen	yence@wustl.edu	Washington University St. Louis
Tom Zega	tzega@lpl.arizona.edu	University of Arizona
Ryan Zeigler	ryan.a.zeigler@nasa.gov	NASA Johnson Space Center
Linda Ziamanesh	lsz9tp@virginia.edu	University of Virginia
Karen Ziegler	kziegler@unm.edu	University of New Mexico

966